
Neural Collapse Under MSE Loss: Proximity to and Dynamics on the Central Path

X.Y. Han*

Cornell University
xh332@cornell.edu

Vardan Papyan*

University of Toronto
vardan.papyan@utoronto.ca

David L. Donoho

Stanford University
donoho@stanford.edu

Abstract

Recent work [Papyan, Han, and Donoho, 2020] discovered a phenomenon called Neural Collapse (NC) that occurs pervasively in today’s deep net training paradigm of driving cross-entropy loss towards zero. In this phenomenon, the last-layer features collapse to their class-means, both the classifiers and class-means collapse to the same Simplex Equiangular Tight Frame (ETF), and the behavior of the last-layer classifier converges to that of the nearest-class-mean decision rule. Since then, follow-ups—such as Mixon et al. [2020] and Poggio and Liao [2020a,b]—formally analyzed this inductive bias by replacing the hard-to-study cross-entropy by the more analytically tractable mean squared error (MSE) loss. But, these works stopped short of demonstrating the empirical reality of MSE-NC on benchmark datasets and canonical networks—as had been done in Papyan, Han, and Donoho [2020] for the cross-entropy loss. In this work, we establish the empirical reality and reproducibility of MSE-NC by reporting experimental observations for three prototypical networks and five canonical datasets—with code for reproducing NC in PyTorch for both MSE and cross-entropy in the following Google Colaboratory notebook: [here](#). Following this, we develop three main contributions inspired by MSE-NC. Firstly, we show a new theoretical decomposition of the MSE loss into (A) a term assuming the last-layer classifier is exactly the least-squares or Webb and Lowe [1990] classifier and (B) a term capturing the deviation from this least-squares classifier. Secondly, we exhibit experiments on canonical datasets and networks demonstrating that, during training, term-(B) is negligible. This motivates a new theoretical construct: the *central path*, where the linear classifier stays MSE-optimal—for the given feature activations—throughout the dynamics. Finally, through our study of continually renormalized gradient flow along the central path, we produce closed-form dynamics that predict full Neural Collapse in an unconstrained features model.

Societal Impact Statement: This work tackles a theoretical subject matter, and so does not present any foreseeable societal consequence.

1 Introduction

Modern deep net training combines a set of practices that amount to a paradigm; some such practices include train/test partitioning, canonical datasets, multi-layered architectures, stochastic gradient descent, batch normalization, cross-entropy loss, and training past zero error towards zero loss. Understanding these practices, their properties, and possible avenues for improvement, is an important task of today’s research community.

*Equal contribution. Listed alphabetically.

1.1 Neural Collapse

In a recent paper, Papayan, Han, and Donoho [2020] expose a striking phenomenon that emerges during the training of multi-class classification deep nets. That phenomenon, **Neural Collapse**, unfolds during the **Terminal Phase of Training** (TPT). During this phase, training proceeds past zero *error*—when error is defined by

$$\text{Error} = \text{Ave}_{i,c} \mathbf{1}\{c \neq \arg \max_{c'} \langle \mathbf{w}_{c'}, \mathbf{h}_{i,c} \rangle + b_{c'}\}$$

—towards zero cross-entropy *loss*—defined by

$$\text{CrossEntropy} = -\text{Ave}_{i,c} \log \frac{\exp\{\langle \mathbf{w}_c, \mathbf{h}_{i,c} \rangle\}}{\sum_{c'=1}^C \exp\{\langle \mathbf{w}_{c'}, \mathbf{h}_{i,c} \rangle\}},$$

where C is the number of classes, $\mathbf{w}_c \in \mathbb{R}^P$ and $b_c \in \mathbb{R}$ denote the c -th class classifier and bias, and $\mathbf{h}_{i,c} \in \mathbb{R}^P$ are the last-layer features of the i -th training example in the c -th class.

Neural Collapse is defined relative to the feature global mean,

$$\boldsymbol{\mu}_G = \text{Ave}_{i,c} \mathbf{h}_{i,c},$$

the feature class-means,

$$\boldsymbol{\mu}_c = \text{Ave}_i \mathbf{h}_{i,c}, \quad c = 1, \dots, C,$$

and the feature within-class covariance,

$$\boldsymbol{\Sigma}_W = \text{Ave}_{i,c} (\mathbf{h}_{i,c} - \boldsymbol{\mu}_c)(\mathbf{h}_{i,c} - \boldsymbol{\mu}_c)^\top.$$

When the dataset is balanced (i.e. when the number of examples per class, N , is equal for all classes²), NC is characterized by the following four limiting behaviors, where the limits take place with increasing training epoch t :

(NC1) Within-class variability collapse:

$$\boldsymbol{\Sigma}_W \rightarrow \mathbf{0}$$

(NC2) Convergence to Simplex ETF:

$$\frac{\langle \boldsymbol{\mu}_c - \boldsymbol{\mu}_G, \boldsymbol{\mu}_{c'} - \boldsymbol{\mu}_G \rangle}{\|\boldsymbol{\mu}_c - \boldsymbol{\mu}_G\|_2 \|\boldsymbol{\mu}_{c'} - \boldsymbol{\mu}_G\|_2} \rightarrow \begin{cases} 1, & c = c' \\ \frac{-1}{C-1}, & c \neq c' \end{cases}$$

$$\|\boldsymbol{\mu}_c - \boldsymbol{\mu}_G\|_2 - \|\boldsymbol{\mu}_{c'} - \boldsymbol{\mu}_G\|_2 \rightarrow 0 \quad \forall c \neq c'$$

(NC3) Convergence to self-duality:

$$\frac{\mathbf{w}_c}{\|\mathbf{w}_c\|_2} - \frac{\boldsymbol{\mu}_c - \boldsymbol{\mu}_G}{\|\boldsymbol{\mu}_c - \boldsymbol{\mu}_G\|_2} \rightarrow \mathbf{0}$$

(NC4): Simplification to nearest class center:

$$\arg \max_{c'} \langle \mathbf{w}_{c'}, \mathbf{h} \rangle + b_{c'} \rightarrow \arg \min_{c'} \|\mathbf{h} - \boldsymbol{\mu}_{c'}\|_2$$

(NC2) captures the convergence to a simple geometric structure called an *equiangular tight frame* (ETF). An ETF is a collection of vectors $\{\mathbf{v}_c\}_{c=1}^C$ having equal lengths and equal pair-wise angles

²Similar to Papayan, Han, and Donoho [2020], we focus on the canonical setting of balanced datasets in this paper. Recent work by Fang et al. [2021] explores NC for imbalanced classes (discussed in Section E.6 of the Supplementary Material).

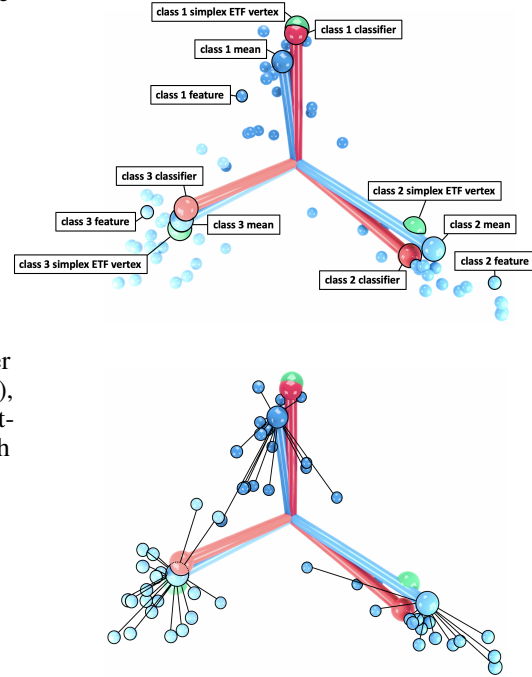


Figure 1: Portrait of Neural Collapse. Top figure depicts the last-layer features, class-means, and classifiers with which NC is defined—as well as the Simplex ETF to which they all converge with training. Bottom figure shows the deviations of features from their corresponding class-means. *Reproduced and modified from Figure 1 of Papayan, Han, and Donoho [2020].*

that are maximally separated. In all modern classification deep nets, the last-layer features are always of dimension larger than the number of classes i.e. $P > C$. In this setting, the maximal pair-wise angles are given by

$$\frac{\langle \mathbf{v}_c, \mathbf{v}_{c'} \rangle}{\|\mathbf{v}_c\|_2 \|\mathbf{v}_{c'}\|_2} = \begin{cases} 1, & \text{for } c = c' \\ -\frac{1}{C-1}, & \text{for } c \neq c' \end{cases},$$

and the ETF is called a Simplex ETF. Observe that as C increases, the Simplex ETF approaches a (partial) orthogonal matrix. Thus, when C is large, this translates to the intuitive notion that classifiers and class-means tend with training to (near) orthogonality.

One interesting consequence of Neural Collapse—pertinent to margin-based approaches for predicting generalization [Bartlett et al., 2017, Neyshabur et al., 2017a,b, Arora et al., 2018, Jiang et al., 2018, 2019, Nagarajan and Kolter, 2019, Wei and Ma, 2019]—is that all margins converge to equality: Banburski et al. [2021] explores this in detail.

1.2 Neural Collapse under MSE loss and the unconstrained features model

While multi-class classification deep nets are typically trained with cross-entropy loss, Demirkaya et al. [2020] and Hui and Belkin [2020] reported that similar test performance is achieved when minimizing the mean squared error (MSE) loss,

$$\begin{aligned} \mathcal{L}(\mathbf{W}, \mathbf{b}, \mathbf{H}) &= \frac{1}{2} \text{Ave}_{i,c} \|\mathbf{W} \mathbf{h}_{i,c} + \mathbf{b} - \mathbf{y}_c\|_2^2 + \frac{\lambda}{2} (\|\mathbf{W}\|_F^2 + \|\mathbf{b}\|_2^2) \\ &= \frac{1}{2NC} \|\mathbf{W} \mathbf{H} + \mathbf{b} \mathbf{1}_{NC}^\top - \mathbf{Y}\|_F^2 + \frac{\lambda}{2} (\|\mathbf{W}\|_F^2 + \|\mathbf{b}\|_2^2). \end{aligned} \quad (1)$$

Above, $\mathbf{H} \in \mathbb{R}^{P \times NC}$ and $\mathbf{Y} \in \mathbb{R}^{C \times NC}$ are obtained by stacking feature vectors $\mathbf{h}_{i,c}$ and one-hot vectors \mathbf{y}_c , respectively, into the columns of a matrix. Moreover, $\mathbf{W} \in \mathbb{R}^{C \times P}$ is obtained by stacking the classifiers \mathbf{w}_c into the rows of a matrix, and $\mathbf{b} \in \mathbb{R}^C$ is obtained by concatenating the scalars $\{b_c\}_{c=1}^C$ into a vector. We denote by $\mathbf{1}_{NC}$ a length- NC vector of ones.

The MSE loss is appealing for its algebraic simplicity, but also because several recent works [Demirkaya et al., 2020, Hui and Belkin, 2020, Poggio and Liao, 2020a,b, Mixon et al., 2020] have called attention to MSE in the classification setting (see Section E of the Supplementary Material for further discussion). In particular, Poggio and Liao [2020a,b]³ recently investigated whether Neural Collapse occurs when training multi-layered homogeneous, weight-normalized networks, for classification under MSE loss (see discussion in Section E.4 of the Supplementary Material). Meanwhile, Mixon et al. [2020] studied the occurrence of Neural Collapse when minimizing the MSE loss in Equation (1) (without weight decay) with gradient flow directly on \mathbf{W} and \mathbf{H} . Mixon et al. call this the *unconstrained features model*, because the features are not constrained to be the output of a deep net forward pass but are rather free variables that can be optimized directly (see discussion in Section E.1 of the Supplementary Material). Concurrently, a different unconstrained features abstraction—albeit for cross-entropy loss—was also proposed by Fang et al. [2021] in their *layered-peeled model* (see discussion in Section E.6 of the Supplementary Material). These very recent contributions provoke an interest in whether Neural Collapse occurs under MSE loss in the deep net setting as well as further careful investigation into the theoretically-attractive unconstrained features framework.

1.3 Contributions

We document here, for the first time, the occurrence of Neural Collapse in five canonical datasets trained on three prototypical networks under MSE loss; see Section 2 and Section A of the Supplementary Material. We then study the optimization dynamics within the unconstrained features model—giving a new approach to understanding those dynamics which focuses attention on a central case for which Neural Collapse is plainly visible in *closed-form*; see Sections 3-4. This differs from the aforementioned work by Mixon et al. [2020], which does not give a closed-form description of the dynamics and also partially relies on a linear-approximation to the underlying ODE.

³In a special section, co-authored with Andrzej Banburski.

In particular, Section 3 decomposes the MSE loss in Equation (1) into two components:

$$\mathcal{L}(\mathbf{W}, \mathbf{b}, \mathbf{H}) = \mathcal{L}_{\text{LS}}(\mathbf{H}) + \mathcal{L}_{\text{LS}}^{\perp}(\mathbf{W}, \mathbf{b}, \mathbf{H}),$$

where

$$\mathcal{L}_{\text{LS}}(\mathbf{H}) = \frac{1}{2} \text{Ave}_{i,c} \|\mathbf{W}_{\text{LS}} \mathbf{h}_{i,c} + \mathbf{b}_{\text{LS}} - \mathbf{y}_c\|_2^2 + \frac{\lambda}{2} (\|\mathbf{W}_{\text{LS}}\|_F^2 + \|\mathbf{b}_{\text{LS}}\|_2^2),$$

and \mathbf{W}_{LS} and \mathbf{b}_{LS} are the least-squares (LS) solutions to Equation (1), so they depend on \mathbf{H} only; and $\mathcal{L}_{\text{LS}}^{\perp}(\mathbf{W}, \mathbf{b}, \mathbf{H})$ visibly measures the deviation of (\mathbf{W}, \mathbf{b}) from $(\mathbf{W}_{\text{LS}}, \mathbf{b}_{\text{LS}})$.

Figure 9 in Section A of the Supplementary Material shows that $\mathcal{L}_{\text{LS}}^{\perp}(\mathbf{W}, \mathbf{b}, \mathbf{H})$ is negligible compared to $\mathcal{L}_{\text{LS}}(\mathbf{H})$ during training of canonical deep nets on benchmark datasets. This motivates us to examine, in Section 4, the subset of all possible classifier-feature tuples called the **central path**,

$$\mathcal{P} = \{(\mathbf{W}_{\text{LS}}(\mathbf{H}), \mathbf{b}_{\text{LS}}(\mathbf{H}), \mathbf{H}) \mid \mathbf{H} \in \mathbb{R}^{P \times NC}\}, \quad (2)$$

for which $\mathcal{L}_{\text{LS}}^{\perp}(\mathbf{W}, \mathbf{b}, \mathbf{H}) = 0$; the notation $\mathbf{W}_{\text{LS}}(\mathbf{H}), \mathbf{b}_{\text{LS}}(\mathbf{H})$ makes explicit the fact that the optimal classifier and bias are functions of \mathbf{H} *only*. It follows that, on the central path, the loss (\mathcal{L}) also depends on \mathbf{H} only. We will call \mathcal{L}_{LS} and $\mathcal{L}_{\text{LS}}^{\perp}$ the *central path* and *deviation* components, respectively. From this perspective, Figure 9 indicates that the classifiers and features in deep nets approach the central-path early in training.

Section 4 further identifies the *invariance property* that $\mathcal{L}_{\text{LS}}(\mathbf{H}) = \mathcal{L}_{\text{LS}}(\mathbf{A}\mathbf{H})$ for *any* positive-definite matrix \mathbf{A} ; thus, inducing an equivalence-class of features. Among all \mathbf{A} , choosing $\mathbf{A} = \Sigma_W^{-\frac{1}{2}}$ leads us to focus on the *renormalized features*, $\mathbf{X} = \Sigma_W^{-\frac{1}{2}} \mathbf{H}$ — i.e. the representer possessing an identity within-class covariance. This, in turn, inspires the *continuously renormalized gradient flow* on the central path:

$$\frac{d}{dt} \mathbf{X} = -\Pi_{T_{\mathbf{X}} \mathcal{X}} (\nabla_{\mathbf{X}} \mathcal{L}_{\text{LS}}(\mathbf{X})), \quad (3)$$

where the operator $\Pi_{T_{\mathbf{X}} \mathcal{X}}$ projects the gradient onto the manifold, \mathcal{X} , of all identity-covariance features. We not only show that this flow induces the convergence of classifier-features tuples, $(\mathbf{W}, \mathbf{b}, \mathbf{H}) \in \mathcal{P}$, to Neural Collapse, but also derive a closed-form solution of the dynamics. The solution is *explicit* in terms of the singular values and the singular vectors of the renormalized class-means at initialization.

Our contributions include a further decomposition of \mathcal{L}_{LS} ,

$$\mathcal{L}_{\text{LS}}(\mathbf{H}) = \mathcal{L}_{\text{NC1}}(\mathbf{H}) + \mathcal{L}_{\text{NC2/3}}(\mathbf{H}).$$

Convergence of \mathcal{L}_{NC1} to zero visibly implies (NC1), while convergence to zero of $\mathcal{L}_{\text{NC2/3}}$ visibly implies (NC2) and (NC3).

2 Empirical observations of Neural Collapse under MSE loss

We complement this paper with an extensive series of measurements on five canonical datasets⁴ (MNIST, FashionMNIST, SVHN, CIFAR10, and STL10) and three prototypical networks (VGG, ResNet, and DenseNet). Since these experiments each occupy sizable three-by-five arrays—all together spanning almost four pages—all measurements described in this section, along with their experimental and training details, are collectively presented in Section A of the Supplementary Material. This section surveys their results.

Empirical evidence of MSE Neural Collapse. First, to solidify the foundations of NC research in the MSE setting, we present—in Figures 2-8 and Table 1—experiments showing that the phenomena observed by Papayan, Han, and Donoho [2020] for cross-entropy loss also occur when training using MSE loss. Then, supplementing the theoretical analysis in Section 3, we show, in Figure 9, the empirical-decomposition of the MSE loss into interpretable terms.

⁴The choice of these datasets is motivated by Demirkaya et al. [2020], Hui and Belkin [2020] and is discussed in Section A.1 of the Supplementary Material.

MSE loss vs. Cross-Entropy loss. We discovered that the networks trained with MSE loss tend to achieve faster activation collapse than those trained with cross-entropy reported by Pappayan, Han, and Donoho [2020]. Additionally, robustness tends to be better—sometimes several magnitudes better—when the network is trained with MSE loss than with cross-entropy loss. These findings are demonstrated in Figures 10 and 11, respectively.

3 Decomposition of MSE loss

Motivated by the community’s interest in the role of the MSE loss in deep net training [Mixon et al., 2020, Poggio and Liao, 2020a,b, Demirkaya et al., 2020, Hui and Belkin, 2020], we derive a new decomposition of the MSE loss that gives insights into the NC phenomenon. First, absorb the bias vector into the weight matrix—by defining the extended weight matrix $\tilde{\mathbf{W}} = [\mathbf{W}, \mathbf{b}] \in \mathbb{R}^{C \times (P+1)}$ and the extended feature vector $\tilde{\mathbf{h}}_{i,c} = [\mathbf{h}_{i,c}; 1] \in \mathbb{R}^{P+1}$ —so that the loss in Equation (1) can be written concisely as follows:

$$\mathcal{L}(\tilde{\mathbf{W}}, \tilde{\mathbf{H}}) = \frac{1}{2} \text{Ave}_{i,c} \|\tilde{\mathbf{W}} \tilde{\mathbf{h}}_{i,c} - \mathbf{y}_c\|_2^2 + \frac{\lambda}{2} \|\tilde{\mathbf{W}}\|_F^2. \quad (4)$$

Relative to the extended features, $\{\tilde{\mathbf{h}}_{i,c}\}$, we define the statistics $\tilde{\boldsymbol{\mu}}_G$, $\tilde{\boldsymbol{\mu}}_c$, and $\tilde{\boldsymbol{\Sigma}}_W$ analogously to those in Section 1.1. We further define the total covariance matrix:

$$\tilde{\boldsymbol{\Sigma}}_T = \text{Ave}_{i,c} (\tilde{\mathbf{h}}_{i,c} - \tilde{\boldsymbol{\mu}}_G)(\tilde{\mathbf{h}}_{i,c} - \tilde{\boldsymbol{\mu}}_G)^\top.$$

Let $\tilde{\mathbf{M}}$ denote the $P \times C$ matrix with extended class-means, $\tilde{\boldsymbol{\mu}}_c$, as its columns. Reformulating the results of Webb and Lowe [1990], with weight decay incorporated, gives the following result.

Proposition 1 (Webb and Lowe [1990] with weight decay). *For a fixed set of features, $\tilde{\mathbf{H}}$, the optimal classifier, $\tilde{\mathbf{W}}$, minimizing the MSE loss, $\mathcal{L}(\tilde{\mathbf{W}}, \tilde{\mathbf{H}})$, is*

$$\tilde{\mathbf{W}}_{LS} = \frac{1}{C} \tilde{\mathbf{M}}^\top (\tilde{\boldsymbol{\Sigma}}_T + \lambda \mathbf{I})^{-1}.$$

$\tilde{\mathbf{W}}_{LS}$ is an MSE-optimal classifier, depending on the augmented features $\tilde{\mathbf{H}}$ only, based on which we identify a new decomposition of the MSE loss.

Theorem 1. *The MSE loss, $\mathcal{L}(\tilde{\mathbf{W}}, \tilde{\mathbf{H}})$, can be decomposed into two terms, $\mathcal{L}(\tilde{\mathbf{W}}, \tilde{\mathbf{H}}) = \mathcal{L}_{LS}(\tilde{\mathbf{H}}) + \mathcal{L}_{LS}^\perp(\tilde{\mathbf{W}}, \tilde{\mathbf{H}})$, where*

$$\mathcal{L}_{LS}(\tilde{\mathbf{H}}) = \frac{1}{2} \text{Ave}_{i,c} \|\tilde{\mathbf{W}}_{LS} \tilde{\mathbf{h}}_{i,c} - \mathbf{y}_c\|_2^2 + \frac{\lambda}{2} \|\tilde{\mathbf{W}}_{LS}\|_F^2,$$

and

$$\mathcal{L}_{LS}^\perp(\tilde{\mathbf{W}}, \tilde{\mathbf{H}}) = \frac{1}{2} \text{tr} \left\{ (\tilde{\mathbf{W}} - \tilde{\mathbf{W}}_{LS}) \left(\tilde{\boldsymbol{\Sigma}}_T + \tilde{\boldsymbol{\mu}}_G \tilde{\boldsymbol{\mu}}_G^\top + \lambda \mathbf{I} \right) (\tilde{\mathbf{W}} - \tilde{\mathbf{W}}_{LS})^\top \right\}.$$

Proof. Given in Section B of the Supplementary Material. \square

The component $\mathcal{L}_{LS}^\perp(\tilde{\mathbf{W}}, \tilde{\mathbf{H}})$ is non-negative⁵ and is zero only when $\tilde{\mathbf{W}} = \tilde{\mathbf{W}}_{LS}$. Therefore, $\mathcal{L}_{LS}^\perp(\tilde{\mathbf{H}})$ quantifies the distance of $\tilde{\mathbf{W}}$ from $\tilde{\mathbf{W}}_{LS}$. In short, the *central path* component, $\mathcal{L}_{LS}(\tilde{\mathbf{H}})$, captures the behavior of the network when the classifier possesses optimal, least squares behavior, while the *deviation* component, $\mathcal{L}_{LS}^\perp(\tilde{\mathbf{W}}, \tilde{\mathbf{H}})$, captures the divergence from that behavior.

We can further decompose $\mathcal{L}_{LS}(\tilde{\mathbf{H}})$ into two terms, one capturing activation collapse (NC1) and the other capturing convergence to Simplex ETF of both features and classifiers (NC2 and NC3).

Theorem 2. *The central path component, $\mathcal{L}_{LS}(\tilde{\mathbf{H}})$, of the MSE decomposition in Theorem 1 can be further decomposed into $\mathcal{L}_{LS}(\tilde{\mathbf{H}}) = \mathcal{L}_{NC1}(\tilde{\mathbf{H}}) + \mathcal{L}_{NC2/3}(\tilde{\mathbf{H}})$, where*

$$\mathcal{L}_{NC1}(\tilde{\mathbf{H}}) = \frac{1}{2} \text{tr} \left\{ \tilde{\mathbf{W}}_{LS} \left(\tilde{\boldsymbol{\Sigma}}_W + \lambda \mathbf{I} \right) \tilde{\mathbf{W}}_{LS}^\top \right\},$$

and

$$\mathcal{L}_{NC2/3}(\tilde{\mathbf{H}}) = \frac{1}{2C} \|\tilde{\mathbf{W}}_{LS} \tilde{\mathbf{M}} - \mathbf{I}\|_F^2.$$

⁵The middle term is the sum of positive-semidefinite matrices—one of which is positive-definite.

Proof. Given in Section C of the Supplementary Material. \square

Inspection of these terms is revealing. For example, \mathcal{L}_{NCI} is characterized by its within-class covariance term—implying that it measures the deviations of last-layer features from class-means. For it to tend to zero, individual activations would need to tend to their corresponding class-means. See further discussion of these terms in Section C.2 of the Supplementary Material.

4 Exact closed-form analysis on central path

For conciseness, we consider $\lambda = 0$ in this Section 4. We now state our main result:

Theorem 3. *In the unconstrained features model, start from an initial features matrix with zero global mean, restrict to the central path within a manifold where features are normalized to identity within-class covariance, and follow gradient flow on the objective \mathcal{L}_{LS} . Then, Neural Collapse emerges on the renormalized features with explicit dynamics of the flow given in Proposition 2 as well as Corollaries 1 and 2 later in this paper.*

Three assumptions stand out, which we discuss below:

(A1) Restriction to central path: Figure 9 of the Supplementary Material shows that—in practice, during TPT— $\mathcal{L}_{\text{LS}}^\perp(\tilde{\mathbf{W}}, \tilde{\mathbf{H}})$ is observed to be negligible compared to the dominant term, $\mathcal{L}_{\text{LS}}(\tilde{\mathbf{H}})$. This, in turn, implies that $(\tilde{\mathbf{W}}, \tilde{\mathbf{H}})$ is close to the central path (defined in Equation 2) since, for tuples on the central path, $\mathcal{L}_{\text{LS}}^\perp(\tilde{\mathbf{W}}, \tilde{\mathbf{H}}) = 0$.

(A2) Zero global mean: The above-described proximity to the central path also implies that the last-layer biases become close to \mathbf{b}_{LS} . From Webb and Lowe [1990], we know that

$$\mathbf{b}_{\text{LS}} = C^{-1}\mathbf{1} - C^{-1}\bar{\mathbf{M}}^\top \Sigma_T^{-1}\boldsymbol{\mu}_G.$$

Notice that the prediction errors obey

$$\begin{aligned} \mathbf{W}_{\text{LS}}\mathbf{h} + \mathbf{b}_{\text{LS}} - \mathbf{y} &= C^{-1}\mathbf{M}^\top \Sigma_T^{-1}\mathbf{h} + C^{-1}\mathbf{1} - C^{-1}\bar{\mathbf{M}}^\top \Sigma_T^{-1}\boldsymbol{\mu}_G - \mathbf{y} \\ &= C^{-1}\mathbf{M}^\top \Sigma_T^{-1}(\mathbf{h} - \boldsymbol{\mu}_G) - (\mathbf{y} - C^{-1}\mathbf{1}), \end{aligned}$$

where the last line exhibits two terms in parentheses, both traceable to the action of the bias \mathbf{b}_{LS} . The term $\mathbf{h} - \boldsymbol{\mu}_G$ demonstrates that the bias induces a global-mean subtraction on \mathbf{h} , while the term $\mathbf{y} - C^{-1}\mathbf{1}$ demonstrates that the bias also induces a global-mean subtraction on the targets. Thus, the features effectively have zero global mean.

(A3) Renormalization to identity covariance: Renormalization is ideologically preceded in the theoretical ML literature by works such as Banburski et al. [2019], Poggio and Liao [2020a,b]—which normalized the weight norms of homogeneous deep nets to one—as well as in earlier works such as Douglas et al. [1998]. Within this paper, the covariance-renormalization is inspired by an invariance property of the loss as well as the intuitive concept of the signal-to-noise ratio from mathematical statistics; a detailed discussion of both follows soon in Sections 4.1 and 4.2.

In the following subsections, we describe the most meaningful abstractions and results leading to the proof of Theorem 3. The full derivations are deferred to Section D of the Supplementary Material.

4.1 Invariance property

Given Assumption (A2), we can represent the central path (defined in Equation 2) in terms of globally mean-subtracted activations.

Definition 1 (Zero Global Mean Central Path).

$$\bar{\mathcal{P}} = \left\{ (\mathbf{W}_{\text{LS}}, \bar{\mathbf{H}}) \mid \mathbf{W}_{\text{LS}} = C^{-1}\bar{\mathbf{M}}^\top \Sigma_T^{-1} \right\},$$

where $\bar{\mathbf{H}} \in \mathbb{R}^{P \times NC}$ has columns $\mathbf{h}_{i,c} - \boldsymbol{\mu}_G$.

An important *invariance property* holds on the central path: Let \mathbf{A} denote a symmetric positive-definite matrix. Then,

$$\mathbf{W}_{\text{LS}}(\mathbf{A}\bar{\mathbf{H}})\mathbf{A}\bar{\mathbf{H}} = \mathbf{W}_{\text{LS}}(\bar{\mathbf{H}})\mathbf{A}^{-1}\mathbf{A}\bar{\mathbf{H}} = \mathbf{W}_{\text{LS}}(\bar{\mathbf{H}})\bar{\mathbf{H}}.$$

In short, the actual predictions made by the least squares classifier are invariant to choice of the coordinates in which we express $\bar{\mathbf{H}}$, i.e. all features $\mathbf{A}\bar{\mathbf{H}}$ are *equivalently performing*. Among those coordinate systems, we will prefer the one in which the “noise” is “whitened” or “sphered.”

Suppose that Σ_W is invertible and consider transforming the activations to new coordinates $\bar{\mathbf{H}} \mapsto \mathbf{A}\bar{\mathbf{H}}$ using $\mathbf{A} = \Sigma_W^{-\frac{1}{2}}$, where we use symmetric square roots throughout. In these coordinates, the features are renormalized: the within-class covariance becomes $\Sigma_W(\mathbf{A}\bar{\mathbf{H}}) = \mathbf{A}\Sigma_W(\bar{\mathbf{H}})\mathbf{A} = \mathbf{I}$, and the globally centered class-means matrix becomes $\bar{\mathbf{M}}(\mathbf{A}\bar{\mathbf{H}}) = \mathbf{A}\bar{\mathbf{M}}(\bar{\mathbf{H}}) = \Sigma_W^{-\frac{1}{2}}(\bar{\mathbf{H}})\bar{\mathbf{M}}(\bar{\mathbf{H}})$. The class-means of these *renormalized features* evoke the clarifying signal-to-noise ratio perspective from mathematical statistics, which we explore in the next subsection. Additional implications and interpretations of invariance are given in Section D.2 of the Supplementary Material.

4.2 Signal-to-Noise ratio matrix on the central path

Henceforth, we consider the situation where the features have both zero-global-mean and full-rank. Notice the least-squares classifier may then be written as follows:

$$\mathbf{W}_{\text{LS}} = \mathbf{C}^{-1}\bar{\mathbf{M}}^\top(\Sigma_B + \Sigma_W)^{-1} = \mathbf{C}^{-1}\bar{\mathbf{M}}^\top\left(\mathbf{C}^{-1}\bar{\mathbf{M}}\bar{\mathbf{M}}^\top + \Sigma_W\right)^{-1}.$$

The combined presence of the terms $\bar{\mathbf{M}}\bar{\mathbf{M}}^\top$ and Σ_W in the denominator, along with $\bar{\mathbf{M}}$ in the numerator, signals to us the presence of an important quantity which we will call the *signal-to-noise (SNR) ratio matrix* defined as follows:

Definition 2 (Signal-to-Noise Ratio (SNR) Matrix).

$$\text{SNR} \equiv \Sigma_W^{-\frac{1}{2}}\bar{\mathbf{M}}.$$

Why this terminology? The globally-centered class-means represent the overall “signal” indicating that the classes are separated from each other: if they were non-separated, e.g. all equal, $\bar{\mathbf{M}}$ would be zero. However, a classifier decision must keep in view noise—captured by Σ_W —which might confuse the classifier. So, one wishes the signal be large compared to the noise. It may help to consider the mental model—which is not at all necessary to the correctness of our analysis—under which the activations are normally distributed with $\mathbf{h}_{i,c} \sim \mathcal{N}(\mu_c, \Sigma_W)$. Under that model, a linear classifier will indeed get confused if the norm $\|\mu_c - \mu_G\|_2$ is “small compared” to Σ_W . Replacing this somewhat vague statement by a discussion of quantitative properties of the SNR matrix is well understood by mathematical statisticians to be decisive for understanding classification performance in the normal case. In the context of Section 4.1, $\text{SNR} = \bar{\mathbf{M}}(\Sigma_W^{-\frac{1}{2}}\bar{\mathbf{H}})$; in other words, *the SNR matrix is simply the class-means matrix of the renormalized features*.

The most relevant quantitative properties of the SNR matrix are captured by its singular value decomposition (SVD).

Definition 3 (SVD of SNR Matrix).

$$\text{SNR} = \mathbf{U}\mathbf{\Omega}\mathbf{V}^\top = \sum_{j=1}^{C-1} \omega_j \mathbf{u}_j \mathbf{v}_j^\top.$$

Here, the matrices \mathbf{U} and \mathbf{V} are partial orthogonal and orthogonal, respectively—each having C columns with $\mathbf{U}^\top\mathbf{U} = \mathbf{I}_C = \mathbf{V}^\top\mathbf{V}$. Notice that the rank of the SNR matrix is at most $C - 1$ since the matrix of the global-mean-subtracted class-means, $\bar{\mathbf{M}}$, is of rank $C - 1$.

The non-zero singular values, $\{\omega_j\}_{j=1}^{C-1}$, are decisive for understanding the separation performance of the least-squares linear classifier. Good performance demands that they be large; indeed the smallest one controls the orthogonal distance of each class-mean from the linear span of the other class-means. Consequently, driving-larger the smallest nonzero singular value makes the task of linear separation more immune to (spherical) noise and to Euclidean-norm-constrained adversarial noise. Moreover, on the central path, *the MSE loss depends only on the singular values of the SNR matrix*:

Lemma 1 (Spectral Representation of MSE Loss). *On the central path, the MSE loss obeys*

$$\mathcal{L}(\mathbf{W}_{\text{LS}}(\bar{\mathbf{H}}), \bar{\mathbf{H}}) = \mathcal{L}_{\text{LS}}(\mathbf{W}_{\text{LS}}(\bar{\mathbf{H}}), \bar{\mathbf{H}}) = \frac{1}{2} \sum_{j=1}^{C-1} \frac{1}{\omega_j^2 + C} = \mathcal{L}(\{\omega_j\}_{j=1}^{C-1}),$$

and its decomposition obeys

$$\begin{aligned}\mathcal{L}_{NC1}(\bar{\mathbf{H}}) &= \frac{1}{2} \sum_{j=1}^{C-1} \frac{\omega_j^2}{(C + \omega_j^2)^2} = \mathcal{L}_{NC1}(\{\omega_j\}_{j=1}^{C-1}) \\ \mathcal{L}_{NC2/3}(\bar{\mathbf{H}}) &= \frac{1}{2} \sum_{j=1}^{C-1} \frac{1}{C} \left(\frac{\omega_j^2}{\omega_j^2 + C} - 1 \right)^2 = \mathcal{L}_{NC2/3}(\{\omega_j\}_{j=1}^{C-1}).\end{aligned}$$

Proof. Given in Section D.1 of the Supplementary Material. \square

4.3 Dynamics of SNR

We now present Proposition 2, Corollary 1, and Corollary 2, which collectively make up Theorem 3.

Proposition 2 (Dynamics of Singular Values of SNR Matrix). *Continuously renormalized gradient flow on the central path (defined in Equation 3) induces the following closed-form dynamics on the singular values of the renormalized class-means i.e. the SNR matrix:*

$$c_1 \log(\omega_j(t)) - c_2 \log(\omega_j^2(t) + c_3) + c_4 \omega_j^2(t) = a_j + t, \quad t \geq 0. \quad (5)$$

c_1, c_2, c_3 , and c_4 are positive constants independent of j , and a_j is a constant depending on j .

Proof. Given in Section D.5 of the Supplementary Material. \square

From Proposition 2, we can deduce the following limiting behaviors of $\omega_j(t)$:

Corollary 1 (Properties of Solution). *Singular values $\omega_j(t)$ following the dynamics described in Equation (5) satisfy the following limiting behaviors:*

1. $\lim_{t \rightarrow \infty} \omega_j(t) = \infty$
2. $\lim_{t \rightarrow \infty} \frac{\omega_j(t)}{\sqrt{\frac{t}{c_4}}} = 1$
3. $\lim_{t \rightarrow \infty} \frac{\max_j \omega_j(t)}{\min_j \omega_j(t)} = 1$

Proof. As t tends to infinity, the right-hand side of Equation (5) diverges to infinity and therefore so does the left-hand side (LHS). As the LHS approaches infinity, the logarithmic terms become negligible compared to the dominant quadratic term, implying $\omega_j^2(t) \rightarrow \infty$. Since $\omega_j(t)$ are singular values, they must be non-negative—implying $\omega_j(t) \rightarrow \infty$. Based on the same argument, observe that $\lim_{t \rightarrow \infty} \frac{\omega_j(t)}{\sqrt{\frac{t}{c_4}}} = 1$ for all j . Since the constant c_4 is independent of j , it follows that

$$\lim_{t \rightarrow \infty} \frac{\max_j \omega_j(t)}{\min_j \omega_j(t)} = 1. \quad \square$$

Corollary 1 then allows us to deduce the occurrence of Neural Collapse:

Corollary 2 (Neural Collapse Under MSE Loss). *Continuously renormalized gradient flow on the central path leads to Neural Collapse i.e. (NC1)-(NC4). In particular, the SNR matrix converges to*

$$\lim_{t \rightarrow \infty} \frac{1}{\omega_{\max}(t)} \text{SNR}_t = \mathbf{U}_0 \mathbf{V}_0^\top, \quad (6)$$

and the renormalized features matrix converges to

$$\lim_{t \rightarrow \infty} \frac{1}{\omega_{\max}(t)} \Sigma_{W,t}^{-\frac{1}{2}} \bar{\mathbf{H}}_t = (\mathbf{U}_0 \mathbf{V}_0^\top) \otimes \mathbf{I}_N, \quad (7)$$

where \mathbf{U}_0 and \mathbf{V}_0 are the left and right singular vectors of the SNR matrix corresponding to the non-zero singular values at initialization and $\omega_{\max}(t)$ is the largest singular value at time t .

Proof. Consider the normalized SNR matrix $\frac{1}{\omega_{\max}(t)}\text{SNR}_t$ at time t . Corollary 1 proves the singular values $j = 1, \dots, C - 1$ of SNR_t diverge to infinity and that their ratio tends to one. (The C -th singular value is 0 due to the zero global-mean.) Hence, (every convergent subsequence of) $\frac{1}{\omega_{\max}(t)}\text{SNR}_t$ converges to a Simplex ETF. This gives (NC2).

Lemma 1 shows that the MSE loss on the central path depends only on the singular values, and not on the singular vectors, of the matrices SNR_t and Ω_t . As a result, the gradient of $\mathcal{L}(\omega(t))$ does not depend on the singular vectors of these matrices. Thus, the renormalized gradient flow will not change the singular vectors of these matrices, and we get the limit in Equation (6).

Based on Equation (6), we deduce the within-class covariance, $\Sigma_W \left(\frac{1}{\omega_{\max}(t)} \mathbf{X}_t \right)$, becomes negligible compared to the between-class covariance. Therefore, the normalized matrix $\frac{1}{\omega_{\max}(t)} \mathbf{X}_t$ undergoes activation collapse (NC1). From Theorem 1 of Pappan, Han, and Donoho [2020], we then know that (NC3) and (NC4) follow from (NC1) and (NC2).

Combining the limit in Equation (6) with (NC1) proves the limit in Equation (7). \square

5 Discussion

5.1 Related NC works

Since the publication of Pappan, Han, and Donoho [2020], several works [Mixon et al., 2020, Lu and Steinerberger, 2020, E and Wojtowysch, 2020, Poggio and Liao, 2020a,b, Fang et al., 2021, Ergen and Pilanci, 2020, Zhu et al., 2021] proposed mathematical derivations and frameworks ratifying the empirical facts of Neural Collapse. In Section E of the Supplementary Material, we survey each of these very recent papers—which are currently only available in preprint. Presumably these are not yet peer-reviewed and so they might ultimately appear with very different claims or results.

5.2 Limitations

In the analysis in Section 4 (combined with the full-details in Section D of the Supplementary Material), we renormalize the features to have an identity within-class covariance. For renormalized features, we prove that continuously renormalized gradient flow converges to Neural Collapse. This model is the first among the proposed abstractions exhibiting Neural Collapse [Mixon et al., 2020, Poggio and Liao, 2020a, Lu and Steinerberger, 2020, E and Wojtowysch, 2020] that provides insightful closed-form expressions for the dynamics, as given in Proposition 2 and Corollary 1.

The continually renormalized gradient flow on MSE loss—just like the other models surveyed in Section E—provide an abstract setting with which to understand the behaviors of Neural Collapse. Neither the model presented in this work nor the models proposed by the aforementioned related works are sacrosanct: In today’s dominant machine learning paradigm, the features are very particularly constrained, not unconstrained. Namely, they are produced by the output of a forward pass through numerous layers within complex architectures. Yet, this gap between abstractions and today’s standard deep net architectures should not be interpreted as reason to doubt the relevance of Neural Collapse itself, which—as demonstrated by the extensive experiments in Section A for MSE loss and by Pappan, Han, and Donoho [2020] for cross-entropy loss—is an empirical fact on numerous datasets and deep nets. Rather, these theoretical results—especially the novel closed-form expressions in Proposition 2 and Corollary 1—are a first step towards using mathematical abstraction to gain insight into the nature of the phenomena.

6 Conclusion

We empirically showed that Neural Collapse occurs when classification deep nets are trained with MSE loss on canonical deep nets and datasets. We then derived and measured a novel decomposition of the MSE loss. We observed that the last-layer classifier tends to the least-squares classifier early in training—motivating us to define the central path on which the classifier behaves exactly as optimal least-squares classifier. On the central path, we showed invariance properties that inspired us to examine the renormalized features and their corresponding continuously renormalized gradient flow. This flow induces closed-form dynamics that imply the occurrence of Neural Collapse.

Acknowledgements: We thank the Stanford Research Computing Center for providing computational resources and support that enabled our research.

References

- Sanjeev Arora, Rong Ge, Behnam Neyshabur, and Yi Zhang. Stronger generalization bounds for deep nets via a compression approach. In *International Conference on Machine Learning*, pages 254–263. PMLR, 2018.
- Sanjeev Arora, Simon Du, Wei Hu, Zhiyuan Li, and Ruosong Wang. Fine-grained analysis of optimization and generalization for overparameterized two-layer neural networks. In *International Conference on Machine Learning*, pages 322–332. PMLR, 2019.
- Andrzej Banburski, Qianli Liao, Brando Miranda, Lorenzo Rosasco, Fernanda De La Torre, Jack Hidary, and Tomaso Poggio. Theory iii: Dynamics and generalization in deep networks. *arXiv preprint arXiv:1903.04991*, 2019.
- Andrzej Banburski, Fernanda De La Torre, Nishka Plant, Ishana Shastri, and Tomaso Poggio. Cross-validation stability of deep networks. Technical report, Center for Brains, Minds and Machines (CBMM), 2021.
- Peter Bartlett, Dylan J Foster, and Matus Telgarsky. Spectrally-normalized margin bounds for neural networks. *arXiv preprint arXiv:1706.08498*, 2017.
- Lenaic Chizat and Francis Bach. On the global convergence of gradient descent for over-parameterized models using optimal transport. *Advances in neural information processing systems*, 31:3036–3046, 2018.
- Lenaic Chizat and Francis Bach. Implicit bias of gradient descent for wide two-layer neural networks trained with the logistic loss. *arXiv preprint arXiv:2002.04486*, 2020.
- Ahmet Demirkaya, Jiasi Chen, and Samet Oymak. Exploring the role of loss functions in multiclass classification. In *2020 54th Annual Conference on Information Sciences and Systems (CISS)*, pages 1–5. IEEE, 2020.
- Scott C Douglas, SY Kung, and Shun-ichi Amari. A self-stabilized minor subspace rule. *IEEE Signal Processing Letters*, 5(12):328–330, 1998.
- Weinan E and Stephan Wojtowytsch. On the emergence of tetrahedral symmetry in the final and penultimate layers of neural network classifiers. *arXiv preprint arXiv:2012.05420*, 2020.
- Tolga Ergen and Mert Pilanci. Revealing the structure of deep neural networks via convex duality. *arXiv preprint arXiv:2002.09773*, 2020.
- Cong Fang, Hangfeng He, Qi Long, and Weijie J Su. Layer-peeled model: Toward understanding well-trained deep neural networks. *arXiv preprint arXiv:2101.12699*, 2021.
- Kaiming He, Xiangyu Zhang, Shaoqing Ren, and Jian Sun. Delving deep into rectifiers: Surpassing human-level performance on imagenet classification. In *Proceedings of the IEEE international conference on computer vision*, pages 1026–1034, 2015.
- Like Hui and Mikhail Belkin. Evaluation of neural architectures trained with square loss vs cross-entropy in classification tasks. *arXiv preprint arXiv:2006.07322*, 2020.
- Yiding Jiang, Dilip Krishnan, Hossein Mobahi, and Samy Bengio. Predicting the generalization gap in deep networks with margin distributions. *arXiv preprint arXiv:1810.00113*, 2018.
- Yiding Jiang, Behnam Neyshabur, Hossein Mobahi, Dilip Krishnan, and Samy Bengio. Fantastic generalization measures and where to find them. *arXiv preprint arXiv:1912.02178*, 2019.
- Jianfeng Lu and Stefan Steinerberger. Neural collapse with cross-entropy loss. *arXiv preprint arXiv:2012.08465*, 2020.

- Song Mei, Andrea Montanari, and Phan-Minh Nguyen. A mean field view of the landscape of two-layer neural networks. *Proceedings of the National Academy of Sciences*, 115(33):E7665–E7671, 2018.
- Dustin G Mixon, Hans Parshall, and Jianzong Pi. Neural collapse with unconstrained features. *arXiv preprint arXiv:2011.11619*, 2020.
- Vaishnavh Nagarajan and J Zico Kolter. Uniform convergence may be unable to explain generalization in deep learning. *arXiv preprint arXiv:1902.04742*, 2019.
- Behnam Neyshabur, Srinadh Bhojanapalli, David McAllester, and Nathan Srebro. Exploring generalization in deep learning. *arXiv preprint arXiv:1706.08947*, 2017a.
- Behnam Neyshabur, Srinadh Bhojanapalli, and Nathan Srebro. A pac-bayesian approach to spectrally-normalized margin bounds for neural networks. *arXiv preprint arXiv:1707.09564*, 2017b.
- Vardan Papyan, X. Y. Han, and David L. Donoho. Prevalence of Neural Collapse during the terminal phase of deep learning training. *Proceedings of the National Academy of Sciences*, 117(40):24652–24663, 2020.
- Tomaso Poggio and Qianli Liao. Explicit regularization and implicit bias in deep network classifiers trained with the square loss. *arXiv preprint arXiv:2101.00072*, 2020a.
- Tomaso Poggio and Qianli Liao. Implicit dynamic regularization in deep networks. Technical report, Center for Brains, Minds and Machines (CBMM), 2020b.
- Grant M Rotskoff and Eric Vanden-Eijnden. Parameters as interacting particles: long time convergence and asymptotic error scaling of neural networks. In *Proceedings of the 32nd International Conference on Neural Information Processing Systems*, pages 7146–7155, 2018.
- James Townsend. Differentiating the singular value decomposition. Technical report, Technical Report 2016, <https://j-towns.github.io/papers/svd-derivative...>, 2016.
- Andrew R Webb and David Lowe. The optimised internal representation of multilayer classifier networks performs nonlinear discriminant analysis. *Neural Networks*, 3(4):367–375, 1990.
- Colin Wei and Tengyu Ma. Improved sample complexities for deep neural networks and robust classification via an all-layer margin. In *International Conference on Learning Representations*, 2019.
- Zhihui Zhu, Tianyu Ding, Jinxin Zhou, Xiao Li, Chong You, Jeremias Sulam, and Qing Qu. A geometric analysis of neural collapse with unconstrained features. *arXiv preprint arXiv:2105.02375*, 2021.

Neural Collapse Under MSE Loss: Proximity to and Dynamics on the Central Path

Contents of Appendix

A	MSE Neural Collapse experiments	13
A.1	Datasets	13
A.2	Networks	13
A.3	Optimization methodology	13
A.4	Computational resources	13
A.5	Formatting	13
A.6	Exceptions: STL10-ResNet and STL10-DenseNet	14
A.7	Experimental results	14
A.8	Open Questions: Weight-decay, batch normalization, SGD, generalization, test data	20
B	Theorem 1	21
C	Theorem 2	22
C.1	Return to unextended coordinates	22
C.2	Further discussion	22
D	Theorem 3 (and other details)	23
D.1	Lemma 1	23
D.2	Implications of invariance	24
D.3	Aligned SNR coordinates	25
D.4	Continuously renormalized gradient flow	26
D.5	Proof of Proposition 2 (gradient flow in aligned SNR coordinates)	27
E	Related works examining Neural Collapse	29
E.1	Mixon, Parshall, and Pi [2020]	29
E.2	Lu and Steinerberger [2020]	30
E.3	E and Wojtowytsch [2020]	30
E.4	Poggio and Liao [2020a,b] (with Banburski)	30
E.5	Ergen and Pilanci [2020]	30
E.6	Fang, He, Long, and Su [2021]	31
E.7	Zhu, Ding, Zhou, Li, You, Sulam, and Qu [2021]	31

A MSE Neural Collapse experiments

The experiments in this section examine the properties of Neural Collapse (NC) on deep nets trained using MSE loss, and parallel those in Papayan, Han, and Donoho [2020] for deep nets trained with cross-entropy loss. Table 1 and Figures 2-11 show the experimental results with discussion in the captions. See Section 2 of the main text for a high-level overview of these results. Formatting and experimental details are described in Subsections A.1-A.5.

A.1 Datasets

We consider the MNIST, FashionMNIST, CIFAR10, SVHN, and STL10 datasets with pre-processing the same as in Papayan, Han, and Donoho [2020].

A.1.1 Choice of datasets

Demirkaya et al. [2020] and Hui and Belkin [2020] showed multi-class classification deep nets trained with MSE loss—sometimes with a heuristical-scaling—demonstrate comparable test-error performance to those trained with cross-entropy. Even without additional scaling, i.e. with vanilla MSE loss, we found this true for ten class classification datasets—such as MNIST, FashionMNIST, SVHN, CIFAR10, and STL10—so we focus on these five datasets. For more than ten classes, both Demirkaya et al. [2020] and Hui and Belkin [2020] showed that the additional scaling-heuristic does need to be applied to the loss before comparable test-performance can be achieved. In exploratory experiments not reported here, we were able to reproduce their results on datasets with more than ten classes. We feel these scaling-heuristics merit further scientific investigation of their own and are beyond the scope of this article, so we do not include datasets requiring scaling-parameter tuning.

A.2 Networks

We train VGG, ResNet, and DenseNet models with the same depth-selection procedures and architecture-specification choices as in Papayan, Han, and Donoho [2020]. In the MSE setting, the final chosen depths were as follows:

DATASET	VGG	RESNET	DENSENET
MNIST	VGG11	RESNET18	DENSENET40
FASHIONMNIST	VGG11	RESNET18	DENSENET250
SVHN	VGG13	RESNET34	DENSENET40
CIFAR10	VGG11	RESNET50	DENSENET100
STL10	VGG11	RESNET18	DENSENET201

A.3 Optimization methodology

The optimization algorithm, parameters, and hyperparameter tuning are the same as in Papayan, Han, and Donoho [2020].

A.4 Computational resources

The experiments were run on our institutional High-Performance Computing (HPC) cluster. Each dataset-network combination was trained on a single GPU attached to a CPU with at least 32GB of RAM—the specific types of the CPUs/GPUs vary according to whichever was first assigned to us by the HPC cluster scheduler.

A.5 Formatting

The coloring and formatting of the plots are the same as in Papayan, Han, and Donoho [2020].

A.6 Exceptions: STL10-ResNet and STL10-DenseNet

The STL10-ResNet and STL10-DenseNet dataset-network pairs stand out among the experiments described in this section—sometimes displaying outlier behavior either by converging more slowly to Neural Collapse or by exhibiting trends inconsistent with those found in other dataset-network pairs.

STL10 stands apart from the other canonical datasets for multiple reasons⁶ and is a “less-typical” benchmark compared to more “compulsory” datasets like CIFAR10. In this particular case, we hypothesize that its outlier behavior might be caused by the size of the STL10 images (96×96 compared to the 32×32 , after padding, of the other datasets)—leading to a higher-dimensional problem, which, in turn, induces a harder non-convex optimization problem, which might make SGD less likely to converge to a useful optimum or might make the convergence much slower and harder to observe under a fixed computational budget.

It was previously noted in Hui and Belkin [2020] and Demirkaya et al. [2020] that more challenging classification problems—in those projects, problems with more classes to be labeled—may require modifications to the MSE loss. We decided that such modifications are unnecessary in the ten class problems studied in the experiments of this section. But perhaps the outlier nature of the STL10-ResNet and STL10-DenseNet combinations signal that the MSE loss modifications proposed by Hui and Belkin [2020] and Demirkaya et al. [2020] ought to have been used.

A.7 Experimental results

Table 1: Table comparing test-accuracy at moment 0-error is achieved vs. at the end of training. Analogous to Table 1 of Papayan, Han, and Donoho [2020]. The median improvement is 0.962 percentage points; the mean is 1.833 percentage points.

DATASET	NET	ACC. 0-ERROR	ACC. FINAL
MNIST	VGG	99.23	99.59
	RESNET	99.16	99.70
	DENSENET	99.62	99.70
FASHION	VGG	92.76	92.95
	RESNET	93.55	93.76
	DENSENET	90.56	92.95
SVHN	VGG	89.35	93.91
	RESNET	85.18	92.65
	DENSENET	95.61	95.23
CIFAR10	VGG	83.13	84.54
	RESNET	75.43	76.39
	DENSENET	91.77	91.78
STL10	VGG	60.43	67.24
	RESNET	59.35	60.56
	DENSENET	58.74	60.41

⁶For example, one sense in which STL-10 is clearly different from the other datasets is the comparatively small number of labeled training examples per class.

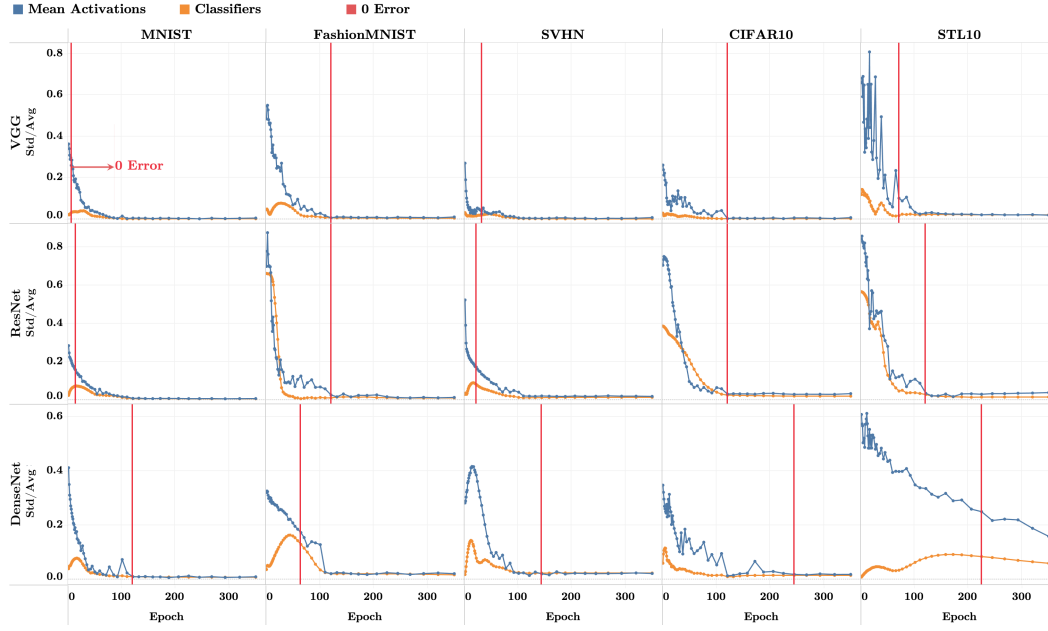


Figure 2: Plots analogous to Figure 2 in Pappan et al. [2020], but on networks trained with MSE Loss. Results demonstrate that last-layer features and classifiers approach *equinormness*.

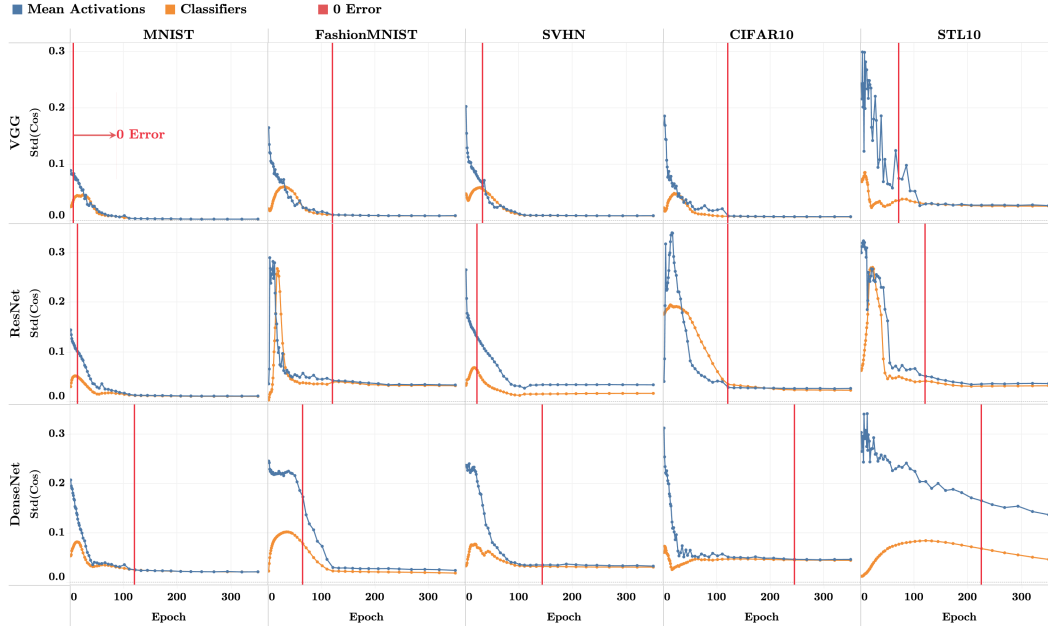


Figure 3: Plots analogous to Figure 3 in Pappan et al. [2020], but on networks trained with MSE Loss. Results demonstrate that last-layer features and classifiers approach *equiangularity*.

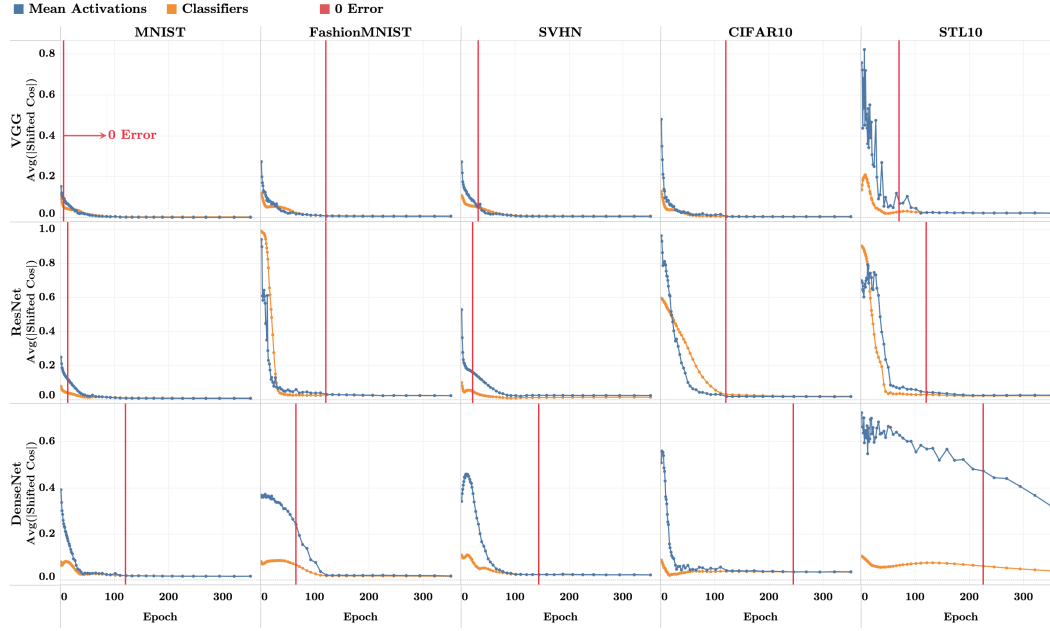


Figure 4: Plots analogous to Figure 4 in Pappan et al. [2020], but on networks trained with MSE Loss. Results demonstrate that last-layer features and classifiers approach *maximal-equiangularity*.

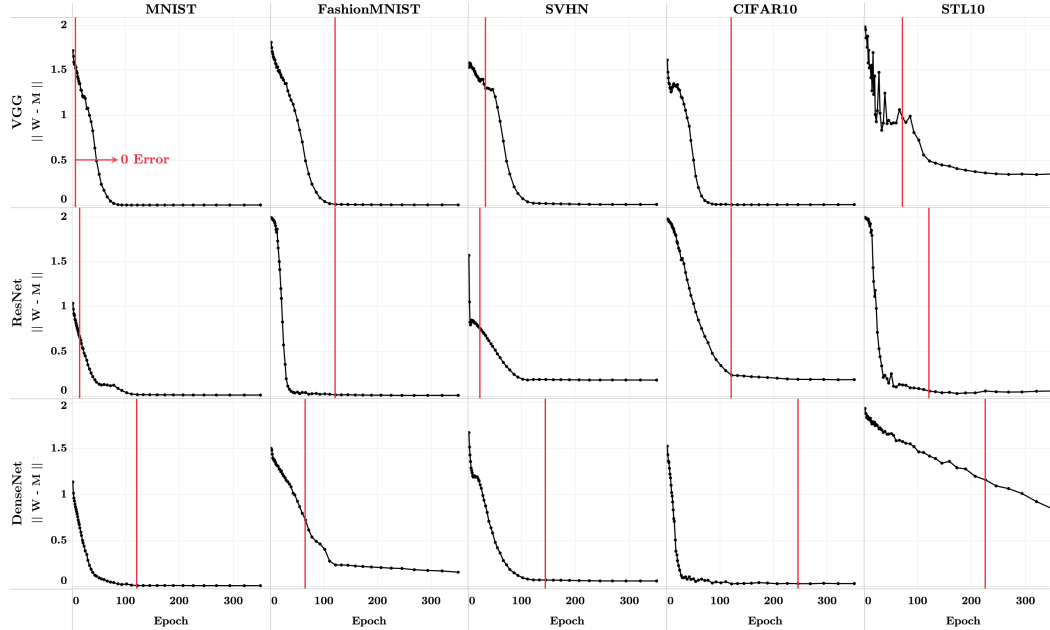


Figure 5: Plots analogous to Figure 5 in Pappan et al. [2020], but on networks trained with MSE Loss. Results demonstrate that last-layer features and classifiers approach *self-duality*.

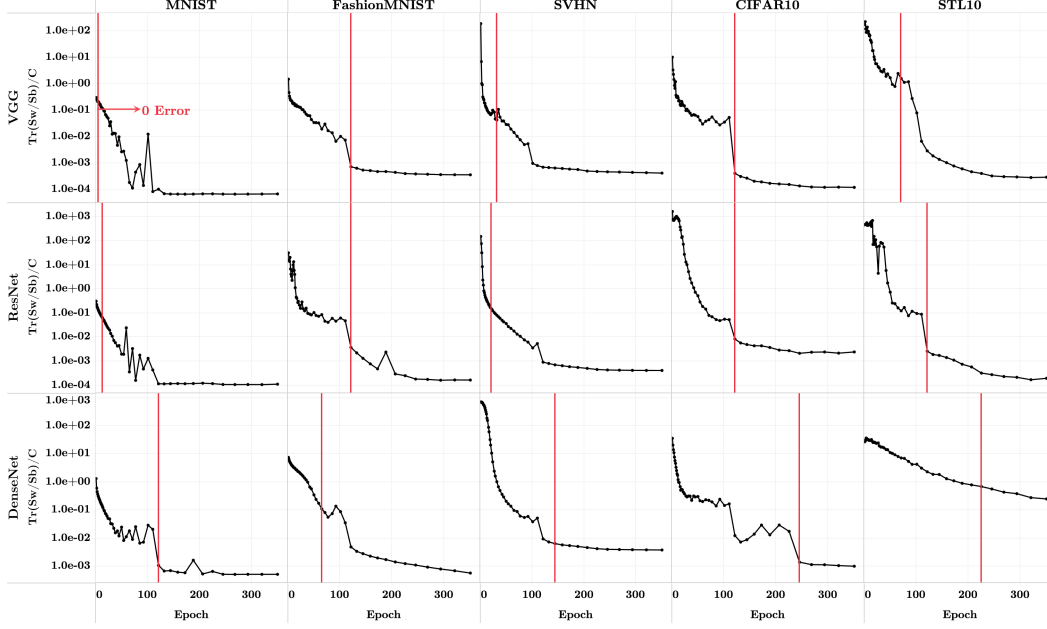


Figure 6: Plots analogous to Figure 6 in Pappan et al. [2020], but on networks trained with MSE Loss. Results demonstrate that last-layer features undergo *variability collapse*.

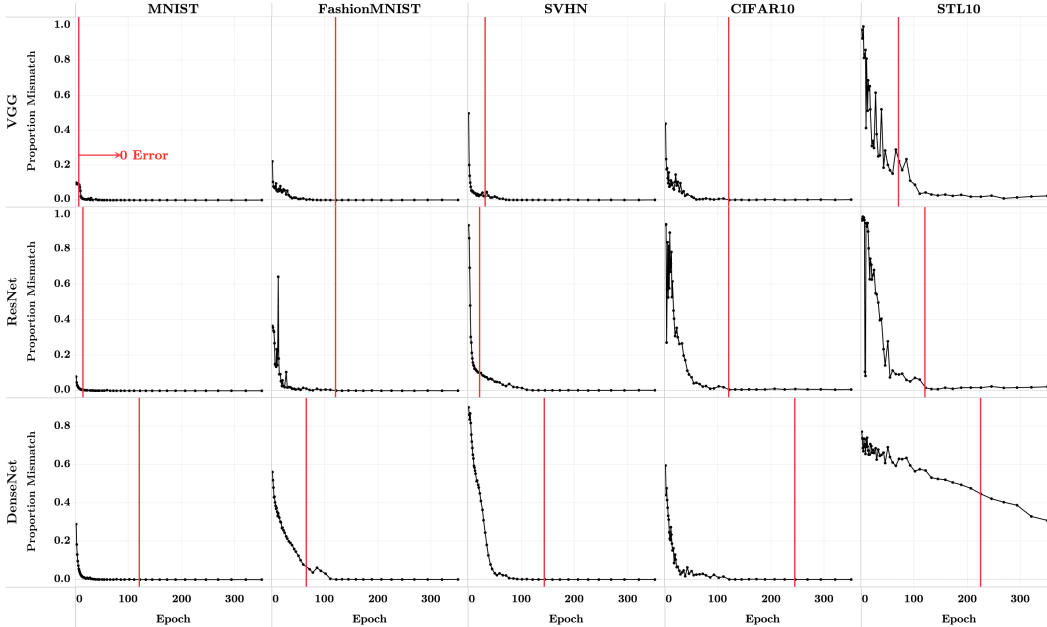


Figure 7: Plots analogous to Figure 7 in Pappan et al. [2020], but on networks trained with MSE Loss. Results demonstrate that classifier decisions converge to those of the *nearest class center decision rule*.

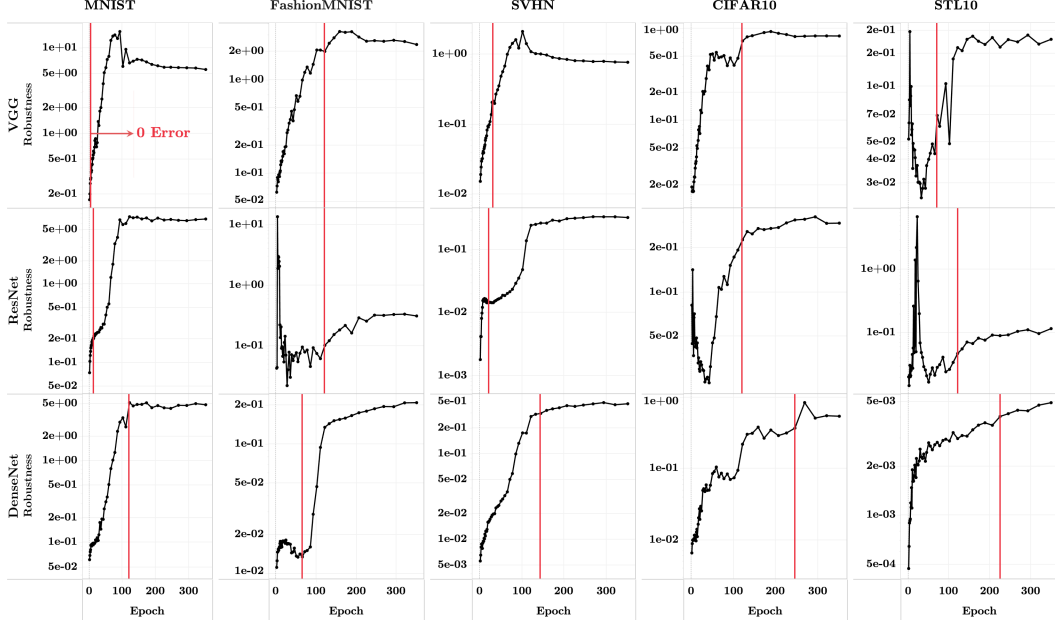


Figure 8: Plots analogous to Figure 8 in Pappan et al. [2020], but on networks trained with MSE Loss. Results demonstrate that networks *become more robust when trained beyond 0-error*. The median improvement in the robustness measure in the last epoch over the first epoch achieving zero training error is 0.1762; the mean improvement is 0.9278.

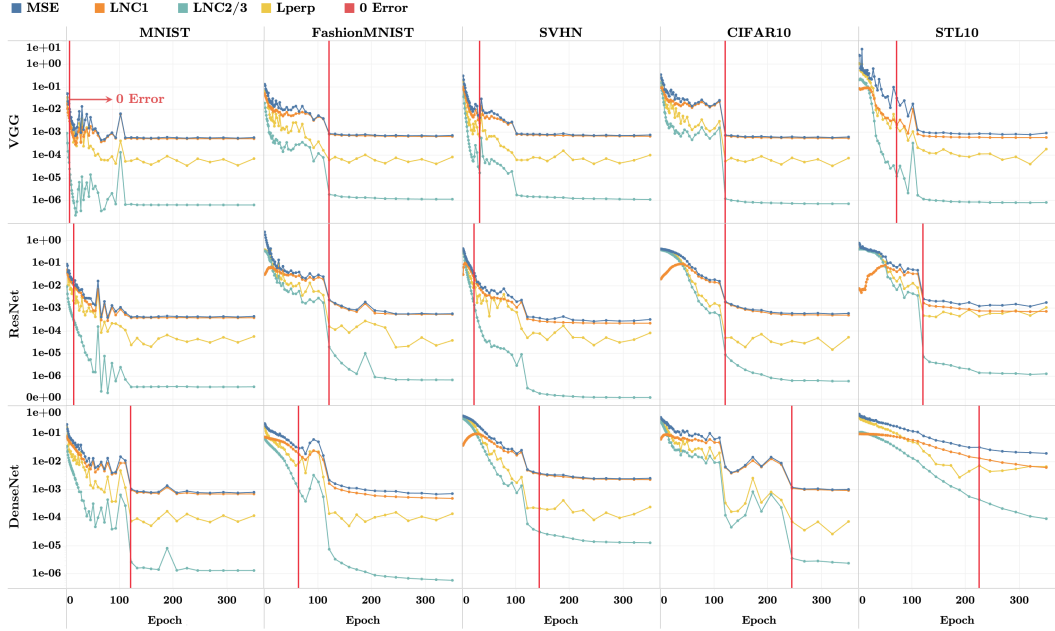


Figure 9: *Decomposition of MSE loss*: In each array cell, we plot the MSE loss, $\mathcal{L}(\tilde{\mathbf{W}}, \tilde{\mathbf{H}})$, and its components, $\mathcal{L}_{\text{NC1}}(\tilde{\mathbf{H}})$, $\mathcal{L}_{\text{NC2/3}}(\tilde{\mathbf{H}})$, and $\mathcal{L}_{\text{LS}}^{\perp}(\tilde{\mathbf{W}}, \tilde{\mathbf{H}})$ which, following the decomposition in Section 3 of the main text, satisfy the relation $\mathcal{L}(\tilde{\mathbf{W}}, \tilde{\mathbf{H}}) = \mathcal{L}_{\text{NC1}}(\tilde{\mathbf{H}}) + \mathcal{L}_{\text{NC2/3}}(\tilde{\mathbf{H}}) + \mathcal{L}_{\text{LS}}^{\perp}(\tilde{\mathbf{W}}, \tilde{\mathbf{H}})$. Observe that, early in the training, $\mathcal{L}_{\text{LS}}^{\perp}(\tilde{\mathbf{W}}, \tilde{\mathbf{H}})$ becomes negligible compared to the dominant term, $\mathcal{L}_{\text{NC1}}(\tilde{\mathbf{H}})$, implying $\mathcal{L}_{\text{LS}}^{\perp}(\tilde{\mathbf{W}}, \tilde{\mathbf{H}}) \ll \mathcal{L}_{\text{LS}}(\tilde{\mathbf{H}}) = \mathcal{L}_{\text{NC1}}(\tilde{\mathbf{H}}) + \mathcal{L}_{\text{NC2/3}}(\tilde{\mathbf{H}})$, i.e. the features and classifiers are *effectively on the central path* during TPT. The STL10-ResNet and STL10-DenseNet display outlier behavior, which we discuss in Section A.6.

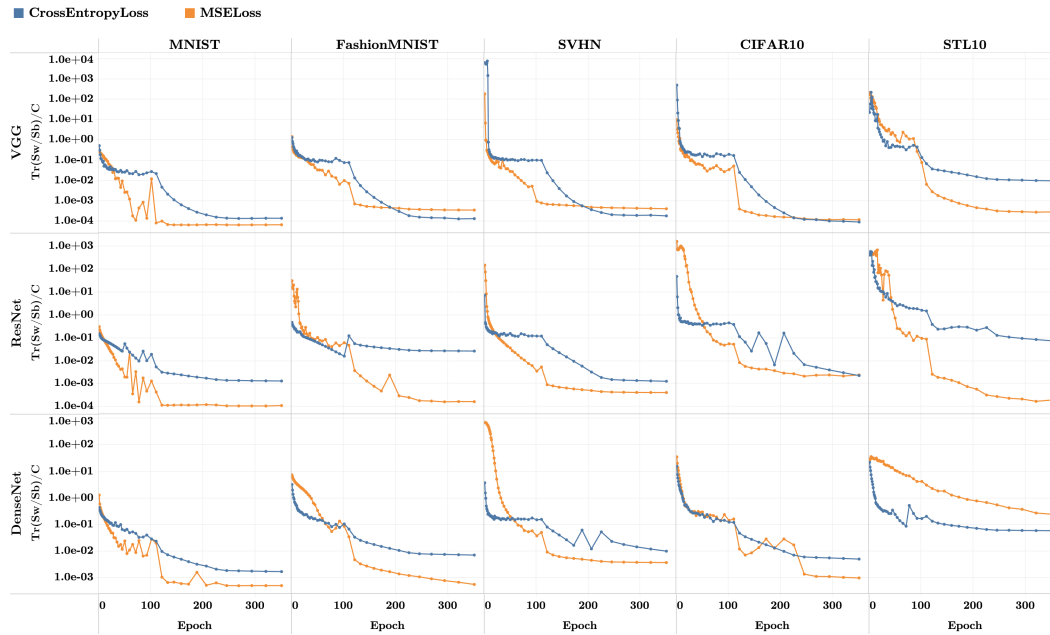


Figure 10: *Activation collapse under MSE loss vs. cross-entropy loss*: Comparison of activation collapse observed in this paper for networks trained under MSE loss (Figure 6) with that observed in Papayan et al. [2020] under cross-entropy loss.

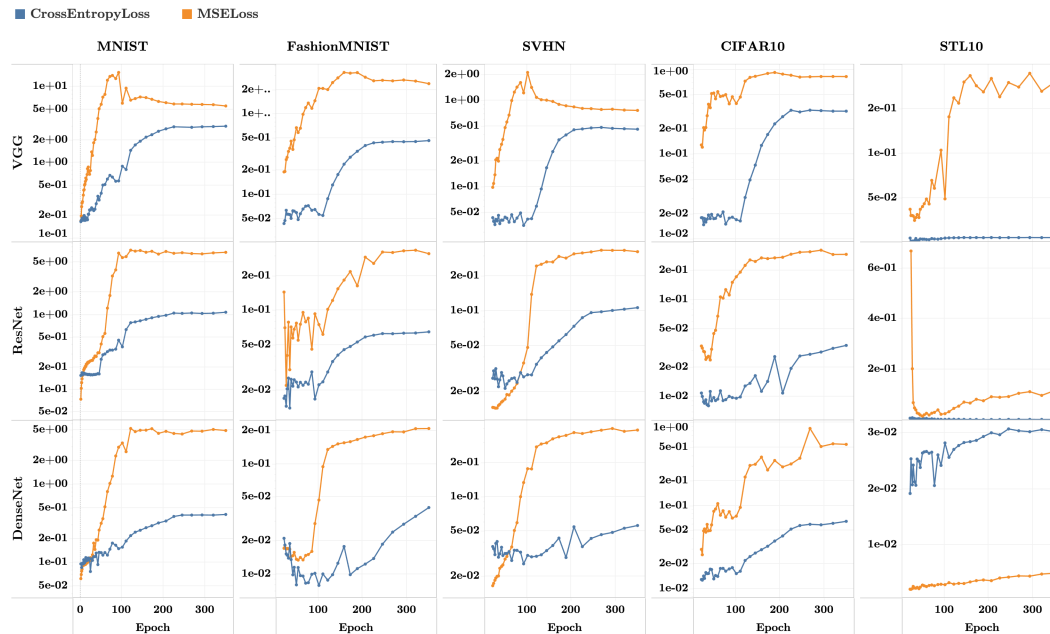


Figure 11: *Adversarial robustness under MSE loss vs. cross-entropy loss*: Comparison of adversarial robustness observed in this paper for networks trained under MSE loss (Figure 8) with that observed in Papayan et al. [2020] under cross-entropy loss.

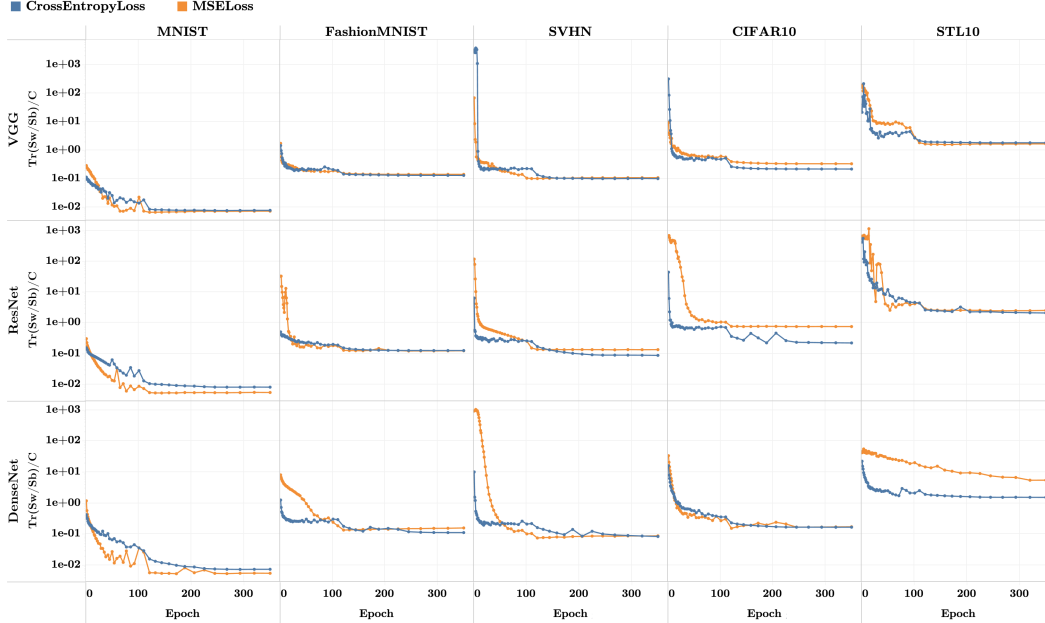


Figure 12: *Activation collapse on test data for both losses*: Activation collapse observed on *test data* for models trained with MSE loss (from this current paper) and cross-entropy loss (posted by Papayan, Han, and Donoho [2020] on Stanford Data Repository). On the test data, activation collapse still visibly occurs on multiple dataset-network combinations: Albeit the rate of collapse is much slower on the test data compared to that on the train data, and the plotted measure (described in Figure 6 of Papayan, Han, and Donoho [2020]) at the last epoch is larger than that on the train data. Also interesting is that the value at the last epoch is roughly monotonic with the difficulty of the dataset. See discussion in Section A.8.

A.8 Open Questions: Weight-decay, batch normalization, SGD, generalization, test data

The experiments in this paper as well as those in Papayan, Han, and Donoho [2020] were conducted under the canonical setting where deep nets were trained using SGD with weight-decay and batch normalization—leading one to wonder about the roles that these particular ingredients play on the NC phenomena. Additionally, most observables focus on the train data—raising the question of how the NC phenomena behave on test data as well as their relationship to generalization. We find these questions intriguing, but feel each deserves careful experimentation outside the scope of this paper.

Nonetheless, we note here that several existing papers have already begun insightful investigations in these directions. For example, weight-decay, weight-normalization (as a proxy for batch-normalization), and SGD play key roles in the analyses of Banburski et al. [2019], Poggio and Liao [2020a,b] that, along other things, lead to the prediction of NC in homogeneous deep nets; also in Banburski et al. [2021], the connection between NC and margin distributions with generalization is also explored.

Another example is Zhu et al. [2021] in which the authors conduct several experiments on ResNets trained on CIFAR10. On their models, the authors examine NC-related properties relative to the train data, test data, and randomly labeled data; they also conducted ablation studies varying control parameters (weight-decay, width, etc.) and the optimization algorithm (SGD, ADAM, L-BFGS). Based on their results, Zhu et al. [2021] propose thought-provoking conjectures on the role of each of these components (see Section E.7 for a brief survey of their findings).

As a preliminary exploration, we include Figure 12 showing the variability collapse (NC1) behavior on *test data* for the networks trained with MSE loss (used in this paper) as well as those trained with cross-entropy loss (released⁷ by Papayan, Han, and Donoho [2020]). From Figure 12, we see that

⁷The cross-entropy test data results were released by Papayan, Han, and Donoho [2020] on the paper’s corresponding Stanford Data Repository entry.

variability collapse occurs much slower on the test data than on the train data. Although not shown here, the other NC phenomena behave similarly.

In this Appendix, we show Figure 12 since it is concise, within reach, and may be of interest to readers who share our curiosity. We refrain from presenting the entire series of multi-figure NC measurements on test data because it is outside the scope of this paper and would significantly lengthen this appendix. We also refrain from speculating on any underlying explanations until more meticulous experiments are conducted.

B Theorem 1

Theorem 1. *The MSE loss, $\mathcal{L}(\tilde{\mathbf{W}}, \tilde{\mathbf{H}})$, can be decomposed into two terms, $\mathcal{L}(\tilde{\mathbf{W}}, \tilde{\mathbf{H}}) = \mathcal{L}_{LS}(\tilde{\mathbf{H}}) + \mathcal{L}_{LS}^\perp(\tilde{\mathbf{W}}, \tilde{\mathbf{H}})$, where*

$$\mathcal{L}_{LS}(\tilde{\mathbf{H}}) = \frac{1}{2} \text{Ave}_{i,c} \|\tilde{\mathbf{W}}_{LS} \tilde{\mathbf{h}}_{i,c} - \mathbf{y}_c\|_2^2 + \frac{\lambda}{2} \|\tilde{\mathbf{W}}_{LS}\|_F^2,$$

and

$$\mathcal{L}_{LS}^\perp(\tilde{\mathbf{W}}, \tilde{\mathbf{H}}) = \frac{1}{2} \text{tr} \left\{ (\tilde{\mathbf{W}} - \tilde{\mathbf{W}}_{LS}) \left(\tilde{\Sigma}_T + \tilde{\mu}_G \tilde{\mu}_G^\top + \lambda I \right) (\tilde{\mathbf{W}} - \tilde{\mathbf{W}}_{LS})^\top \right\}.$$

Proof. Recall the MSE loss:

$$\mathcal{L}(\tilde{\mathbf{W}}, \tilde{\mathbf{H}}) = \frac{1}{2} \text{Ave}_{i,c} \|\tilde{\mathbf{W}} \tilde{\mathbf{h}}_{i,c} - \mathbf{y}_c\|_2^2 + \frac{\lambda}{2} \|\tilde{\mathbf{W}}\|_F^2. \quad (8)$$

Consider a specific extended activations matrix $\tilde{\mathbf{H}}$; the least-squares solution $\tilde{\mathbf{W}}$ minimizing $\mathcal{L}(\tilde{\mathbf{W}}, \tilde{\mathbf{H}})$ with $\tilde{\mathbf{H}}$ kept fixed must obey the following first-order optimality condition:

$$\text{Ave}_{i,c} (\tilde{\mathbf{W}}_{LS} \tilde{\mathbf{h}}_{i,c} - \mathbf{y}_c) \tilde{\mathbf{h}}_{i,c}^\top + \lambda \tilde{\mathbf{W}}_{LS} = 0. \quad (9)$$

From Proposition 1 in the main manuscript, the solution to the above is given by

$$\tilde{\mathbf{W}}_{LS} = C^{-1} \tilde{\mathbf{M}}^\top (\tilde{\Sigma}_T + \lambda I)^{-1}.$$

The loss can be rewritten as

$$\frac{1}{2} \text{Ave}_{i,c} \|\tilde{\mathbf{W}}_{LS} \tilde{\mathbf{h}}_{i,c} - \mathbf{y}_c\|_2^2 + \frac{\lambda}{2} \|\tilde{\mathbf{W}} - \tilde{\mathbf{W}}_{LS}\|_F^2 + \frac{\lambda}{2} \|\tilde{\mathbf{W}}\|_F^2.$$

Combining the above with Equation (9) gives, after rearranging:

$$\frac{1}{2} \text{Ave}_{i,c} \|\tilde{\mathbf{W}}_{LS} \tilde{\mathbf{h}}_{i,c} - \mathbf{y}_c\|_2^2 + \frac{1}{2} \text{Ave}_{i,c} \|(\tilde{\mathbf{W}} - \tilde{\mathbf{W}}_{LS}) \tilde{\mathbf{h}}_{i,c}\|_2^2 - \lambda \text{tr} \left\{ \tilde{\mathbf{W}}_{LS} (\tilde{\mathbf{W}} - \tilde{\mathbf{W}}_{LS})^\top \right\} + \frac{\lambda}{2} \|\tilde{\mathbf{W}}\|_F^2,$$

which is equivalent to

$$\frac{1}{2} \text{Ave}_{i,c} \|\tilde{\mathbf{W}}_{LS} \tilde{\mathbf{h}}_{i,c} - \mathbf{y}_c\|_2^2 + \frac{1}{2} \text{Ave}_{i,c} \|(\tilde{\mathbf{W}} - \tilde{\mathbf{W}}_{LS}) \tilde{\mathbf{h}}_{i,c}\|_2^2 + \frac{\lambda}{2} \|\tilde{\mathbf{W}}_{LS}\|_F^2 + \frac{\lambda}{2} \|\tilde{\mathbf{W}}_{LS} - \tilde{\mathbf{W}}\|_F^2.$$

Using the above, the loss can indeed be decomposed as

$$\mathcal{L}(\tilde{\mathbf{W}}, \tilde{\mathbf{H}}) = \mathcal{L}_{LS}(\tilde{\mathbf{H}}) + \mathcal{L}_{LS}^\perp(\tilde{\mathbf{W}}, \tilde{\mathbf{H}}),$$

where

$$\mathcal{L}_{LS}(\tilde{\mathbf{H}}) \equiv \frac{1}{2} \text{Ave}_{i,c} \|\tilde{\mathbf{W}}_{LS} \tilde{\mathbf{h}}_{i,c} - \mathbf{y}_c\|_2^2 + \frac{\lambda}{2} \|\tilde{\mathbf{W}}_{LS}\|_F^2 \quad (10)$$

and

$$\begin{aligned} \mathcal{L}_{LS}^\perp(\tilde{\mathbf{W}}, \tilde{\mathbf{H}}) &\equiv \frac{1}{2} \text{Ave}_{i,c} \|(\tilde{\mathbf{W}} - \tilde{\mathbf{W}}_{LS}) \tilde{\mathbf{h}}_{i,c}\|_2^2 + \frac{\lambda}{2} \|\tilde{\mathbf{W}}_{LS} - \tilde{\mathbf{W}}\|_F^2 \\ &= \frac{1}{2} \text{tr} \left\{ (\tilde{\mathbf{W}} - \tilde{\mathbf{W}}_{LS}) \left(\tilde{\Sigma}_T + \tilde{\mu}_G \tilde{\mu}_G^\top + \lambda I \right) (\tilde{\mathbf{W}} - \tilde{\mathbf{W}}_{LS})^\top \right\}. \end{aligned}$$

This completes the proof. \square

C Theorem 2

Theorem 2. *The central path component, $\mathcal{L}_{LS}(\tilde{\mathbf{H}})$, of the MSE decomposition in Theorem 1 can be further decomposed into $\mathcal{L}_{LS}(\tilde{\mathbf{H}}) = \mathcal{L}_{NC1}(\tilde{\mathbf{H}}) + \mathcal{L}_{NC2/3}(\tilde{\mathbf{H}})$, where*

$$\mathcal{L}_{NC1}(\tilde{\mathbf{H}}) = \frac{1}{2} \text{tr} \left\{ \tilde{\mathbf{W}}_{LS} \left(\tilde{\Sigma}_W + \lambda \mathbf{I} \right) \tilde{\mathbf{W}}_{LS}^\top \right\},$$

and

$$\mathcal{L}_{NC2/3}(\tilde{\mathbf{H}}) = \frac{1}{2C} \|\tilde{\mathbf{W}}_{LS} \tilde{\mathbf{M}} - \mathbf{I}\|_F^2.$$

Proof. Under Euclidean distance, perturbations to the extended activations matrix $\tilde{\mathbf{H}}$ which affect only the class-means or global-mean are *orthogonal* to perturbations which affect only the within-class covariance. Using this, $\mathcal{L}_{LS}(\tilde{\mathbf{H}})$ can be further decomposed via the Pythagorean theorem:

$$\mathcal{L}_{LS}(\tilde{\mathbf{H}}) = \frac{1}{2} \text{Ave}_{i,c} \|\tilde{\mathbf{W}}_{LS}(\tilde{\mathbf{h}}_{i,c} - \tilde{\boldsymbol{\mu}}_c)\|_2^2 + \frac{\lambda}{2} \|\tilde{\mathbf{W}}_{LS}\|_F^2 + \frac{1}{2} \text{Ave}_c \|\tilde{\mathbf{W}}_{LS} \tilde{\boldsymbol{\mu}}_c - \mathbf{y}_c\|_2^2.$$

The first and second terms above merge into $\mathcal{L}_{NC1}(\tilde{\mathbf{H}})$, while the third term becomes $\mathcal{L}_{NC2/3}(\tilde{\mathbf{H}})$:

$$\begin{aligned} \mathcal{L}_{NC1}(\tilde{\mathbf{H}}) &= \frac{1}{2} \text{tr} \left\{ \tilde{\mathbf{W}}_{LS} \left(\tilde{\Sigma}_W + \lambda \mathbf{I} \right) \tilde{\mathbf{W}}_{LS}^\top \right\} \\ \mathcal{L}_{NC2/3}(\tilde{\mathbf{H}}) &= \frac{1}{2C} \|\tilde{\mathbf{W}}_{LS} \tilde{\mathbf{M}} - \mathbf{I}\|_F^2. \end{aligned} \tag{11}$$

This completes the proof. \square

C.1 Return to unextended coordinates

For intuition, consider when $\lambda = 0$, i.e. the no weight-decay case. Proposition 1 in the main text gives

$$\mathbf{W}_{LS} = C^{-1} \bar{\mathbf{M}}^\top \Sigma_T^{-1}, \tag{12}$$

where $\bar{\mathbf{M}} \in \mathbb{R}^{P \times C}$ is the matrix with columns $\boldsymbol{\mu}_c - \boldsymbol{\mu}_G$. Returning to the unextended coordinates, $\mathcal{L}_{NC1}(\bar{\mathbf{H}})$ simplifies to

$$\mathcal{L}_{NC1}(\bar{\mathbf{H}}) = \frac{1}{2} \text{tr} \left\{ \bar{\mathbf{W}}_{LS} \Sigma_W \bar{\mathbf{W}}_{LS}^\top \right\}, \tag{13}$$

where $\bar{\mathbf{H}} \in \mathbb{R}^{P \times NC}$ has columns $\mathbf{h}_{i,c} - \boldsymbol{\mu}_G$. The term $\mathcal{L}_{NC2/3}(\bar{\mathbf{H}})$ also simplifies instructively to

$$\mathcal{L}_{NC2/3}(\bar{\mathbf{H}}) = \frac{1}{2C} \|\bar{\mathbf{W}}_{LS} \bar{\mathbf{M}} - \Phi\|_F^2, \tag{14}$$

where Φ is the standard Simplex ETF:

$$\Phi = \mathbf{I} - \frac{1}{C} \mathbf{1} \mathbf{1}^\top.$$

C.2 Further discussion

Equations (11) and (13) further evoke the intuition that

$\mathcal{L}_{NC1}(\bar{\mathbf{H}})$ is a variance term that goes to zero only under activation collapse (NC1).

More specifically, we see that, *with the class-means held constant*, the only way to have $\mathcal{L}_{NC1}(\bar{\mathbf{H}}) \rightarrow 0$ is for $\Sigma_W \rightarrow \mathbf{0}$. Similarly, by examining Equation (14), we see that

$\mathcal{L}_{NC2/3}(\bar{\mathbf{H}})$ quantifies deviations of $\bar{\mathbf{W}}_{LS} \bar{\mathbf{M}}$ —i.e. the matrix of class-mean predictions—from the standard Simplex ETF.

Under (NC2) and (NC3), both $\bar{\mathbf{W}}_{LS}$ and $\bar{\mathbf{M}}$ tend to jointly aligned ETF's, possibly in an alternate pose; so $\bar{\mathbf{W}}_{LS} \rightarrow \Phi \mathbf{U}^T$ and $\bar{\mathbf{M}} \rightarrow \mathbf{U} \Phi$ for a partial orthogonal matrix \mathbf{U} satisfying $\mathbf{U}^T \mathbf{U} = \mathbf{I}_C$. Since $\Phi^2 = \Phi$, (NC2) and (NC3) together demand $\bar{\mathbf{W}}_{LS} \bar{\mathbf{M}} \rightarrow \Phi$. Thus, $\mathcal{L}_{NC2/3}(\bar{\mathbf{H}})$ can be interpreted as a semimetric reflecting the distance from achieving (NC2) and (NC3).

D Theorem 3 (and other details)

In Section 4.2, we defined and motivated the SNR matrix and its singular values. For a careful analysis of the dynamics, we first simplify our expression of the SNR matrix by changing basis in both row and column space, namely adopting bases corresponding to the left and right singular vectors, leading to the following definition.

Definition 4 (Aligned SNR Matrix).

$$\Omega = U^\top \Sigma_W^{-\frac{1}{2}} \bar{M} V.$$

As a consequence of the basis change, the aligned SNR matrix is diagonal.

Observation 1 (SVD of Aligned SNR Matrix).

$$\Omega = \sum_{j=1}^{C-1} \omega_j \mathbf{e}_j \mathbf{e}_j^\top$$

In what follows, we refer to the aligned SNR matrix as simply the SNR matrix.

D.1 Lemma 1

With the above definitions, we now show that the loss on the central path can be characterized entirely in terms of the singular values of the SNR matrix i.e. prove Lemma 1.

Lemma 1 (Spectral Representation of MSE Loss). *On the central path, the MSE loss obeys*

$$\mathcal{L}(\mathbf{W}_{LS}(\bar{\mathbf{H}}), \bar{\mathbf{H}}) = \mathcal{L}_{LS}(\mathbf{W}_{LS}(\bar{\mathbf{H}}), \bar{\mathbf{H}}) = \frac{1}{2} \sum_{j=1}^{C-1} \frac{1}{\omega_j^2 + C} = \mathcal{L}(\{\omega_j\}_{j=1}^{C-1}),$$

and its decomposition obeys

$$\begin{aligned} \mathcal{L}_{NCI}(\bar{\mathbf{H}}) &= \frac{1}{2} \sum_{j=1}^{C-1} \frac{\omega_j^2}{(C + \omega_j^2)^2} = \mathcal{L}_{NCI}(\{\omega_j\}_{j=1}^{C-1}) \\ \mathcal{L}_{NC2B}(\bar{\mathbf{H}}) &= \frac{1}{2} \sum_{j=1}^{C-1} \frac{1}{C} \left(\frac{\omega_j^2}{\omega_j^2 + C} - 1 \right)^2 = \mathcal{L}_{NC2B}(\{\omega_j\}_{j=1}^{C-1}). \end{aligned}$$

Proof. Using Equations (12), (13), and (14), the loss on the central path equals

$$\mathcal{L}(\mathbf{W}_{LS}, \bar{\mathbf{M}}) = \frac{1}{2C} \|C^{-1} \bar{\mathbf{M}}^\top \Sigma_T^{-1} \bar{\mathbf{M}} - \Phi\|_F^2 + \frac{1}{2} \text{tr} \left\{ C^{-1} \bar{\mathbf{M}}^\top \Sigma_T^{-1} \Sigma_W \Sigma_T^{-1} \bar{\mathbf{M}} C^{-1} \right\}.$$

Observe $\bar{\mathbf{M}}^\top \Sigma_T^{-1} \bar{\mathbf{M}}$ and Φ are simultaneously diagonalizable since they share the same $[1, \dots, 1]^\top$ null space and Φ has $C - 1$ equal eigenvalues. Thus, the above can be written solely in terms of the SNR matrix Ω :

$$\mathcal{L}(\Omega) = \frac{1}{2C} \left\| \Omega^\top (\Omega \Omega^\top + C I)^{-1} \Omega - I_{C-1} \right\|_F^2 + \frac{1}{2} \text{tr} \left\{ \Omega^\top (\Omega \Omega^\top + C I)^{-2} \Omega \right\},$$

and it can be simplified into

$$\begin{aligned} \mathcal{L}(\omega) &= \frac{1}{2} \sum_{j=1}^{C-1} \frac{1}{C} \left(\frac{\omega_j^2}{\omega_j^2 + C} - 1 \right)^2 + \frac{\omega_j^2}{(C + \omega_j^2)^2} \\ &= \frac{1}{2} \sum_{j=1}^{C-1} \frac{1}{\omega_j^2 + C}. \end{aligned} \tag{15}$$

This completes the proof for Lemma 1. \square

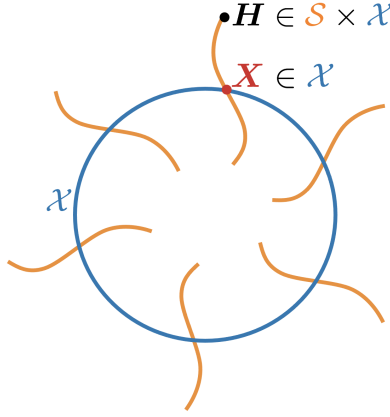


Figure 13: *Fiber bundle*. Any full-rank features matrix, $\bar{\mathbf{H}}$, has a representative element, \mathbf{X} , on \mathcal{X} . For any $\mathbf{X} \in \mathcal{X}$, a *fiber* is the set $\mathcal{S} \times \mathbf{X}$ i.e. $\{\mathbf{A}\mathbf{X} : \mathbf{A} \in \mathcal{S}\}$ (the Minkowski set product), where \mathcal{S} is the set of symmetric positive-definite matrices. Features on the same fiber generate the *same* class predictions and the *same* MSE loss. The optimization described in Sections D.2-D.4 moves *fiber-to-fiber*.

D.2 Implications of invariance

We have seen in Section 4.1 of the main text that, on the central path, both the predictions $\mathbf{W}_{\text{LS}}(\bar{\mathbf{H}})\bar{\mathbf{H}}$ and the MSE loss $\mathcal{L}(\mathbf{W}_{\text{LS}}(\bar{\mathbf{H}}), \bar{\mathbf{M}}(\bar{\mathbf{H}}))$ are invariant under the transformation $\bar{\mathbf{H}} \mapsto \mathbf{A}\bar{\mathbf{H}}$ where \mathbf{A} is a positive-definite matrix.

Consider then the set \mathcal{H} with nonsingular within-class covariances. We view \mathcal{H} as a fiber bundle⁸, where—on each fiber—live (apparently) different activations, $\bar{\mathbf{H}}$, that (in fact) generate the exact *same* class predictions and the exact *same* MSE loss (see Figure 13). The base space—we will denote it \mathcal{X} —can be taken to be the collection of $\mathbf{X} \in \mathcal{H}$ where $\Sigma_W(\mathbf{X}) = \mathbf{I}$. Every $\bar{\mathbf{H}} \in \mathcal{H}$ is representable as $\bar{\mathbf{H}} = \mathbf{A}\mathbf{X}$ where $\mathbf{A} = \Sigma_W^{-\frac{1}{2}}(\bar{\mathbf{H}})$ and $\Sigma_W(\mathbf{X}) = \mathbf{I}$. The activation matrices \mathbf{X} in the base space might be variously called “pre-whitened,” “normalized,” “standardized,” or “sphered.” We shall call \mathcal{X} a *normalized features manifold*⁹.

Invoking invariance, we can make the following observations about our optimization task:

1. If, at a specific t , \mathbf{H}_t happens to be a normalized set of activations (i.e. $\mathbf{H}_t \in \mathcal{X}$ is currently located in the base space \mathcal{X}), there is no performance benefit to leaving the base space. There is also *no performance benefit* to moving *along* a fiber; only by moving from *fiber-to-fiber* can we improve performance.
2. In some sense, we waste time *except* when jumping from fiber-to-fiber; we might prefer to stay in the base space all the time by forcing the dynamics to jump from fiber-to-fiber.

On the other hand, we started with the viewpoint of studying gradient flow of the original \mathbf{H} . So, we consider the following natural model for the application of gradient descent in \mathbf{X} :

1. For a given initial feature activations, $\bar{\mathbf{H}}_0 \in \mathcal{H}$, we renormalize—obtaining a starting point $\mathbf{X}_0 \in \mathcal{X}$; here $\mathbf{X}_0 = \Sigma_W^{-\frac{1}{2}}(\bar{\mathbf{H}}_0)\bar{\mathbf{H}}_0$. Class predictions and MSE loss performance for the MSE-optimal classifier do not change from this renormalization.
2. We compute the usual gradient of MSE loss, at \mathbf{X}_0 , obtaining a step $\Delta\mathbf{X}_0 = -\eta\nabla_{\mathbf{X}}\mathcal{L}_{\text{LS}}(\mathbf{X}_0)$, where η is a step size.

⁸An even larger space could be considered, where $\Sigma_W(\bar{\mathbf{H}})$ is not necessarily full rank, and then other components of this space having covariances of rank C , $C = 1, \dots, 1$ could be considered. We just discuss the full-rank case here.

⁹This is sometimes also called the *Generalized Stiefel Manifold* and will be defined more formally in Section D.3.

3. We take a step, going to

$$\bar{\mathbf{H}}_1 = \mathbf{X}_0 + \Delta \mathbf{X}_0.$$

4. $\bar{\mathbf{H}}_1$ will not necessarily be normalized. We map back along whatever fiber we have landed upon, obtaining a corresponding point in the base space \mathcal{X} , call this \mathbf{X}_1 . Here,

$$\mathbf{X}_1 = \Sigma_W^{-\frac{1}{2}}(\bar{\mathbf{H}}_1)\bar{\mathbf{H}}_1.$$

Class predictions and MSE loss performance do not change from this renormalization.

5. Repeat steps 2, 3, 4 at \mathbf{X}_1 , obtaining thereby \mathbf{X}_2 ; and so on.

This process might be described as *gradient descent with continual renormalization*:

1. Renormalize the initial features activation matrix;
2. Compute the ordinary gradient of MSE loss and take the gradient descent step;
3. Renormalize again after each such step; and
4. Repeat steps 2 and 3.

While the continual renormalization process differs from usual gradient flow, it is both intuitively understandable and sensible; see the discussion in Section 5.2 of the main text.

D.3 Aligned SNR coordinates

More formally, observe that the aligned SNR matrix, $\mathbf{U}^\top \Sigma_W^{-\frac{1}{2}} \bar{\mathbf{M}} \mathbf{V}$, maximally simplifies analysis by reducing the vanilla SNR matrix to a diagonal matrix whose entries determine the MSE loss. We next introduce a comparable alignment of features into their own notion of aligned *SNR coordinates*.

Definition 5 (Renormalization to aligned SNR Coordinates).

$$\mathbf{X} = \mathbf{U}^\top \left(\bar{\mathbf{H}} \mathbf{C} \bar{\mathbf{H}}^\top \right)^{-\frac{1}{2}} \bar{\mathbf{H}} (\mathbf{V} \otimes \mathbf{I}_N),$$

where \otimes is the Kronecker product and \mathbf{C} is a class-centering matrix defined as

$$\mathbf{C} = \frac{1}{NC} \left(\mathbf{I}_{NC} - \frac{1}{N} \mathbf{Y}^\top \mathbf{Y} \right). \quad (16)$$

Intuitively, this implements the renormalization $\mathbf{X} = \Sigma_W^{-\frac{1}{2}} \bar{\mathbf{H}}$ described in Section D.2, followed by a change of basis on both row and column spaces. As discussed in Section 4.1 and Section D.2, this transformation does not change the predictions of the least squares classifier. Hence, it does not change the MSE loss. Moreover, the transformation $\bar{\mathbf{H}} \mapsto \mathbf{X}$ *spheres* the activations by renormalizing them to an \mathbf{X} whose within-class covariance is the identity:

Observation 2 (Sphericity of Within-Class Covariance of SNR Coordinates).

$$\mathbf{X} \mathbf{C} \mathbf{X}^\top = \mathbf{I}$$

Transforming features to the aligned SNR coordinates leads to the following simplification of the aligned SNR matrix (Definition 4):

Observation 3 (Relation Between SNR Coordinates and SNR Matrix).

$$\Omega = \frac{1}{N} \mathbf{X} \mathbf{Y}^\top$$

From a geometric perspective, the transformation in Definition 5 maps the features, \mathbf{H} , to \mathbf{X} belonging to a *Normalized Features Manifold*:

Definition 6 (Normalized Features Manifold).

$$\mathcal{X} = \{ \mathbf{X} \in \mathbb{R}^{C \times NC} \mid \mathbf{X} \mathbf{C} \mathbf{X}^\top = \mathbf{I} \}$$

To understand the dynamics of the singular values of $\mathbf{\Omega}$, we will analyze the gradient flow *on this manifold*. To this end, we first identify its tangent space at a particular \mathbf{X} as well as the projection operator onto that tangent space.

Proposition 3 (Tangent Space of Normalized Features Manifold).

$$T_{\mathbf{X}}\mathcal{X} = \{\mathbf{Z} \in \mathbb{R}^{C \times NC} \mid \mathbf{X}\mathbf{C}\mathbf{Z}^\top + \mathbf{Z}\mathbf{C}\mathbf{X} = \mathbf{0}\}$$

Proposition 4 (Projection Onto Tangent Space of Normalized Features Manifold).

$$\Pi_{T_{\mathbf{X}}\mathcal{X}}(\mathbf{Z}) = \mathbf{Z} - \frac{1}{2}(\mathbf{X}\mathbf{C}\mathbf{Z}^\top + \mathbf{Z}\mathbf{C}\mathbf{X}^\top)\mathbf{X}$$

D.4 Continuously renormalized gradient flow

In Subsection D.2, we described an intuitive algorithm for updating the renormalized features, consisting of a gradient step, $\bar{\mathbf{H}}_1 = \mathbf{X}_0 + \Delta\mathbf{X}_0$ —in Equation (3)—followed by a mapping to the base space of the fiber bundle, $\mathbf{X}_1 = \Sigma(\bar{\mathbf{H}}_1)^{-\frac{1}{2}}\bar{\mathbf{H}}_1$ —in Equation (4). These two steps are in fact equivalent (up to a negligible term) to taking a $T_{\mathbf{X}}\mathcal{X}$ -projected gradient step on the manifold \mathcal{X} as proven below:

Lemma 2. *Assuming $\mathbf{X}_0 \in \mathcal{X}$, a renormalized gradient step,*

$$\mathbf{X}_1 = \Sigma_W^{-\frac{1}{2}}(\bar{\mathbf{H}}_1)\bar{\mathbf{H}}_1 = \Sigma_W^{-\frac{1}{2}}(\mathbf{X}_0 + \Delta\mathbf{X}_0) \cdot (\mathbf{X}_0 + \Delta\mathbf{X}_0),$$

is equivalent, up to an $O(\|\Delta\mathbf{X}_0\|^2)$ term, to a $T_{\mathbf{X}}\mathcal{X}$ -projected gradient step, i.e.

$$\mathbf{X}_1 = \mathbf{X}_0 + \Pi_{T_{\mathbf{X}}\mathcal{X}}(\Delta\mathbf{X}_0) + O(\|\Delta\mathbf{X}_0\|^2).$$

Proof. Notice that

$$\begin{aligned} \mathbf{X}_1 &= \Sigma_W^{-\frac{1}{2}}(\bar{\mathbf{H}}_1)\bar{\mathbf{H}}_1 \\ &= ((\mathbf{X}_0 + \Delta\mathbf{X}_0)\mathbf{C}(\mathbf{X}_0 + \Delta\mathbf{X}_0)^\top)^{-\frac{1}{2}}(\mathbf{X}_0 + \Delta\mathbf{X}_0) \\ &= \left(\mathbf{I} + \Delta\mathbf{X}_0\mathbf{C}\mathbf{X}_0^\top + \mathbf{X}_0\mathbf{C}\Delta\mathbf{X}_0^\top + \Delta\mathbf{X}_0\mathbf{C}\Delta\mathbf{X}_0^\top\right)^{-\frac{1}{2}}(\mathbf{X}_0 + \Delta\mathbf{X}_0), \end{aligned}$$

where in the last step we used our assumption that $\mathbf{X}_0 \in \mathcal{X}$, i.e., $\mathbf{X}_0\mathbf{C}\mathbf{X}_0 = \mathbf{I}$. By Taylor's Theorem,

$$(\mathbf{I} + \mathbf{A})^{-\frac{1}{2}} = \mathbf{I} - \frac{1}{2}\mathbf{A} + O(\|\mathbf{A}\|^2).$$

Therefore, we get

$$\begin{aligned} \mathbf{X}_1 &= \left(\mathbf{I} - \frac{1}{2}(\Delta\mathbf{X}_0\mathbf{C}\mathbf{X}_0^\top + \mathbf{X}_0\mathbf{C}\Delta\mathbf{X}_0^\top + \Delta\mathbf{X}_0\mathbf{C}\Delta\mathbf{X}_0^\top) + O(\|\Delta\mathbf{X}_0\|^2)\right)(\mathbf{X}_0 + \Delta\mathbf{X}_0) \\ &= \mathbf{X}_0 + \Delta\mathbf{X}_0 - \frac{1}{2}(\Delta\mathbf{X}_0\mathbf{C}\mathbf{X}_0^\top + \mathbf{X}_0\mathbf{C}\Delta\mathbf{X}_0^\top)\mathbf{X}_0 + O(\|\Delta\mathbf{X}_0\|^2) \\ &= \mathbf{X}_0 + \Pi_{T_{\mathbf{X}}\mathcal{X}}(\Delta\mathbf{X}_0) + O(\|\Delta\mathbf{X}_0\|^2), \end{aligned}$$

where the last step follows from Proposition 4. \square

As we transition from a discrete gradient descent to a continuous gradient flow, the step size $\eta \rightarrow 0$, and the residual $O(\|\Delta\mathbf{X}_0\|^2)$ in the above lemma becomes negligible, since $\Delta\mathbf{X}_0 = -\eta\nabla_{\mathbf{X}}\mathcal{L}_{\text{LS}}(\mathbf{X}_0)$. This motivates us to study, in the next section, the continuously renormalized gradient flow (as defined in Equation 3 of the main text) of \mathbf{X} on \mathcal{X} :

$$\frac{d}{dt}\mathbf{X} = -\Pi_{T_{\mathbf{X}}\mathcal{X}}(\nabla_{\mathbf{X}}\mathcal{L}_{\text{LS}}(\mathbf{X})).$$

D.5 Proof of Proposition 2 (gradient flow in aligned SNR coordinates)

To prove Proposition 2, we first set up some auxiliary notation and lemmas. Denote the j -th row (transposed) of \mathbf{X} and \mathbf{Y} , respectively, by

$$\mathbf{x}_j = \mathbf{X}^\top \mathbf{e}_j \quad (17)$$

and

$$\mathbf{y}_j = \mathbf{Y}^\top \mathbf{e}_j.$$

Recall that—when differentiating SVDs—the derivative of the j -th singular value, ω_j , only depends on the j -th singular subspace (see Equation 17 of Townsend [2016]). As a consequence, we will see in the following lemma that, for any differential $d\mathbf{X}$, the corresponding $d\omega_j$ only depends on $d\mathbf{x}_j$.

Lemma 3 (Derivative of Singular Values With Respect to SNR Coordinates). *Given the differential 1-form $d\omega_j(\cdot) : T_{\mathbf{X}}\mathcal{X} \rightarrow \mathbb{R}$, the following holds for $d\mathbf{X} \in \mathbb{R}^{C \times NC}$:*

$$d\omega_j(\Pi_{T_{\mathbf{X}}\mathcal{X}}(d\mathbf{X})) = \left(\frac{1}{N} \mathbf{y}_j^\top - \omega_j \mathbf{x}_j^\top \mathbf{C} \right) d\mathbf{x}_j,$$

where $\Pi_{T_{\mathbf{X}}\mathcal{X}}$ denotes the projection onto the tangent space of \mathcal{X} at \mathbf{X} .

Proof. Using Observation 1 and the differential of the singular value decomposition (see Equation 17 of Townsend [2016]):

$$d\omega_j(\Pi_{T_{\mathbf{X}}\mathcal{X}}(d\mathbf{X})) = \mathbf{e}_j^\top d\boldsymbol{\Omega}(\Pi_{T_{\mathbf{X}}\mathcal{X}}(d\mathbf{X})) \mathbf{e}_j, \quad (18)$$

where $d\boldsymbol{\Omega}(\cdot) : T_{\mathbf{X}}\mathcal{X} \rightarrow \mathbb{R}^{C \times C}$ is composed of the differential 1-forms corresponding to each of the entries of $\boldsymbol{\Omega}$. Taking the differential of the expression given in Observation 3, we obtain

$$d\boldsymbol{\Omega}(\mathbf{Z}) = \frac{1}{N} \mathbf{Z} \mathbf{Y}^\top, \quad \forall \mathbf{Z} \in T_{\mathbf{X}}\mathcal{X}.$$

Therefore,

$$d\boldsymbol{\Omega}(\Pi_{T_{\mathbf{X}}\mathcal{X}}(d\mathbf{X})) = \frac{1}{N} \Pi_{T_{\mathbf{X}}\mathcal{X}}(d\mathbf{X}) \mathbf{Y}^\top. \quad (19)$$

Using the projection onto the tangent space, given in Proposition 4 above,

$$\Pi_{T_{\mathbf{X}}\mathcal{X}}(d\mathbf{X}) = d\mathbf{X} - \frac{1}{2} (d\mathbf{X} \mathbf{C} \mathbf{X}^\top + \mathbf{X} \mathbf{C} d\mathbf{X}^\top) \mathbf{X}. \quad (20)$$

Combining Equations (18), (19), and (20), we obtain:

$$\begin{aligned} d\omega_j(\Pi_{T_{\mathbf{X}}\mathcal{X}}(d\mathbf{X})) &= \mathbf{e}_j^\top d\boldsymbol{\Omega}(\Pi_{T_{\mathbf{X}}\mathcal{X}}(d\mathbf{X})) \mathbf{e}_j \\ &= \frac{1}{N} \mathbf{e}_j^\top \Pi_{T_{\mathbf{X}}\mathcal{X}}(d\mathbf{X}) \mathbf{Y}^\top \mathbf{e}_j \\ &= \frac{1}{N} \mathbf{e}_j^\top \left(d\mathbf{X} - \frac{1}{2} (d\mathbf{X} \mathbf{C} \mathbf{X}^\top + \mathbf{X} \mathbf{C} d\mathbf{X}^\top) \mathbf{X} \right) \mathbf{Y}^\top \mathbf{e}_j. \end{aligned} \quad (21)$$

Moreover, using Observation 1 and 3, we can simplify these expressions into

$$\begin{aligned} \frac{1}{N} \mathbf{e}_j^\top d\mathbf{X} \mathbf{Y}^\top \mathbf{e}_j &= \frac{1}{N} \mathbf{y}_j^\top d\mathbf{x}_j \\ \frac{1}{N} \mathbf{e}_j^\top d\mathbf{X} \mathbf{C} \mathbf{X}^\top \mathbf{X} \mathbf{Y}^\top \mathbf{e}_j &= \omega_j \mathbf{e}_j^\top d\mathbf{X} \mathbf{C} \mathbf{X}^\top \mathbf{e}_j = \omega_j \mathbf{x}_j^\top \mathbf{C} d\mathbf{x}_j \\ \frac{1}{N} \mathbf{e}_j^\top \mathbf{X} \mathbf{C} d\mathbf{X}^\top \mathbf{X} \mathbf{Y}^\top \mathbf{e}_j &= \omega_j \mathbf{e}_j^\top \mathbf{X} \mathbf{C} d\mathbf{X}^\top \mathbf{e}_j = \omega_j \mathbf{x}_j^\top \mathbf{C} d\mathbf{x}_j. \end{aligned}$$

Finally, substituting the above three expressions into Equation (21), we get:

$$d\omega_j(\Pi_{T_{\mathbf{X}}\mathcal{X}}(d\mathbf{X})) = \left(\frac{1}{N} \mathbf{y}_j^\top - \omega_j \mathbf{x}_j^\top \mathbf{C} \right) d\mathbf{x}_j,$$

which proves the claim. \square

Using Lemma 3, we can now obtain the dynamics of \mathbf{x}_j under gradient flow:

Lemma 4. *Under continuously renormalized gradient flow (Equation 3),*

$$\frac{d}{dt} \mathbf{x}_j = \frac{\omega_j}{(C + \omega_j^2)^2} \left(\frac{1}{N} \mathbf{y}_j - \omega_j \mathbf{C} \mathbf{x}_j \right).$$

Proof. Recall $\mathbf{x}_j \in \mathbb{R}^{NC}$ is the j -th row of $\mathbf{X} \in \mathbb{R}^{C \times NC}$. Applying the flow definition in Equation 3 to the i -th element of \mathbf{x}_j gives

$$\begin{aligned} \frac{d}{dt} x_{ji} &= -\mathbf{e}_j^\top \Pi_{T_{\mathbf{X}} \mathcal{X}} \left(\frac{d\mathcal{L}_{\text{LS}}}{d\mathbf{X}} \right) \mathbf{e}_i \\ &= -\left\langle \Pi_{T_{\mathbf{X}} \mathcal{X}} \left(\frac{d\mathcal{L}_{\text{LS}}}{d\mathbf{X}} \right), \mathbf{e}_j \mathbf{e}_i^\top \right\rangle_F \\ &= -\left\langle \frac{d\mathcal{L}_{\text{LS}}}{d\mathbf{X}}, \Pi_{T_{\mathbf{X}} \mathcal{X}}(\mathbf{e}_j \mathbf{e}_i^\top) \right\rangle_F, \end{aligned}$$

where $\frac{d\mathcal{L}_{\text{LS}}}{d\mathbf{X}} \in \mathbb{R}^{C \times NC}$ is the standard derivative within the ambient $\mathbb{R}^{C \times NC}$ -space, $\mathbf{e}_i \in \mathbb{R}^{NC}$ and $\mathbf{e}_j \in \mathbb{R}^C$ are the canonical basis vectors, and $\langle \cdot, \cdot \rangle_F$ is the Frobenius matrix inner-product. Next, observe that the differential 1-form $d\mathcal{L}_{\text{LS}}(\cdot) : T_{\mathbf{X}} \mathcal{X} \rightarrow \mathbb{R}$ satisfies the following:

$$d\mathcal{L}_{\text{LS}}(\mathbf{Z}) = \left\langle \frac{d\mathcal{L}_{\text{LS}}}{d\mathbf{X}}, \mathbf{Z} \right\rangle_F, \quad \forall \mathbf{Z} \in T_{\mathbf{X}} \mathcal{X}.$$

Taking $\mathbf{Z} = \Pi_{T_{\mathbf{X}} \mathcal{X}}(\mathbf{e}_j \mathbf{e}_i^\top)$ then leads to

$$\begin{aligned} \frac{d}{dt} x_{ji} &= -d\mathcal{L}_{\text{LS}}(\Pi_{T_{\mathbf{X}} \mathcal{X}}(\mathbf{e}_j \mathbf{e}_i^\top)) \\ &= -\sum_{k=1}^{C-1} \frac{d\mathcal{L}_{\text{LS}}}{d\omega_k} d\omega_k(\Pi_{T_{\mathbf{X}} \mathcal{X}}(\mathbf{e}_j \mathbf{e}_i^\top)) \\ &= -\frac{d\mathcal{L}_{\text{LS}}}{d\omega_j} d\omega_j(\Pi_{T_{\mathbf{X}} \mathcal{X}}(\mathbf{e}_j \mathbf{e}_i^\top)) \end{aligned}$$

where the second step follows by the chain rule, and the last step follows from Lemma 3 in that $d\omega_k(\Pi_{T_{\mathbf{X}} \mathcal{X}}(\mathbf{e}_j \mathbf{e}_i^\top)) = 0$ if $k \neq j$. Moreover, Lemma 3 also gives

$$d\omega_j(\Pi_{T_{\mathbf{X}} \mathcal{X}}(\mathbf{e}_j \mathbf{e}_i^\top)) = \left(\frac{1}{N} \mathbf{y}_j^\top - \omega_j \mathbf{x}_j^\top \mathbf{C} \right) \mathbf{e}_i.$$

It then follows that

$$\begin{aligned} \frac{d}{dt} \mathbf{x}_j &= -\frac{d\mathcal{L}_{\text{LS}}}{d\omega_j} \left(\frac{1}{N} \mathbf{y}_j - \omega_j \mathbf{C} \mathbf{x}_j \right) \\ &= \frac{\omega_j}{(C + \omega_j^2)^2} \left(\frac{1}{N} \mathbf{y}_j - \omega_j \mathbf{C} \mathbf{x}_j \right), \end{aligned}$$

where the last step follows from differentiating the expression in Lemma 1. \square

The gradient flows of \mathbf{x}_j induce the dynamics of ω_j , which are described below.

Lemma 5 (Induced Dynamics on SVD of SNR). *Under continuously renormalized gradient flow (Equation 3),*

$$\frac{d}{dt} \omega_j = \frac{\frac{1}{N} \omega_j + \omega_j^3}{(C + \omega_j^2)^2}. \quad (22)$$

Proof. Applying Lemma 3 and Lemma 4,

$$\frac{d}{dt} \omega_j = \frac{\partial \omega_j}{\partial \mathbf{x}_j} \frac{d\mathbf{x}_j}{dt} = \frac{\omega_j}{(C + \omega_j^2)^2} \left\| \frac{1}{N} \mathbf{y}_j - \omega_j \mathbf{C} \mathbf{x}_j \right\|_2^2,$$

where, for the chain rule, recall that the differential of ω_j only depends on the differential of \mathbf{x}_j (see Lemma 3). Next, using Observation 2:

$$\omega_j^2 \mathbf{x}_j^\top \mathbf{C} \mathbf{x}_j = \omega_j^2.$$

Since $\mathbf{Y} \mathbf{Y}^\top = N \mathbf{I}$,

$$\frac{1}{N^2} \mathbf{y}_j^\top \mathbf{y}_j = \frac{1}{N}.$$

Applying the same relation and Equation (16):

$$\begin{aligned} \frac{2}{N} \omega_j \mathbf{x}_j^\top \mathbf{C} \mathbf{y}_j &= \frac{2}{N} \omega_j \mathbf{e}_j^\top \mathbf{X} \mathbf{C} \mathbf{Y}^\top \mathbf{e}_j \\ &= \frac{1}{NC} \frac{2}{N} \omega_j \mathbf{e}_j^\top \mathbf{X} \left(\mathbf{I} - \frac{1}{N} \mathbf{Y}^\top \mathbf{Y} \right) \mathbf{Y}^\top \mathbf{e}_j = 0. \end{aligned}$$

Combining all the above equations, we obtain

$$\begin{aligned} \frac{d}{dt} \omega_j &= \frac{\omega_j}{(C + \omega_j^2)^2} \left(\frac{1}{N} + \omega_j^2 \right) \\ &= \frac{\frac{1}{N} \omega_j + \omega_j^3}{(C + \omega_j^2)^2}. \end{aligned}$$

□

The closed-form given in Proposition 2 now directly follows.

Proposition 2 (Dynamics of Singular Values of SNR Matrix). *Continuously renormalized gradient flow on the central path (defined in Equation 3) induces the following closed-form dynamics on the singular values of the renormalized class-means i.e. the SNR matrix:*

$$c_1 \log(\omega_j(t)) - c_2 \log(\omega_j^2(t) + c_3) + c_4 \omega_j^2(t) = a_j + t, \quad t \geq 0. \quad (5)$$

c_1, c_2, c_3 , and c_4 are positive constants independent of j , and a_j is a constant depending on j .

Proof. Follows from symbolically solving the ODE in Lemma 5 with routine methods. □

E Related works examining Neural Collapse

In this section, we discuss the contributions and limitations of seven recent works that propose and analyze theoretical abstractions of Neural Collapse. These works are only available in preprint, and may not yet be peer-reviewed. Thus, they might ultimately appear with very different claims or results. Additionally, works such as Poggio and Liao [2020a,b], Ergen and Pilanci [2020] also analyze behaviors other than NC; we will only discuss the parts relevant to Neural Collapse here.

E.1 Mixon, Parshall, and Pi [2020]

Mixon et al. [2020] considered the unconstrained features model in Equation (1) (without weight decay) where, under gradient flow, (\mathbf{W}, \mathbf{H}) evolve according to a nonlinear ordinary differential equation (ODE). They followed a two-step strategy for studying Neural Collapse. First, they linearized the ODE—claiming nonlinear terms are negligible for models initialized near the origin—and proved the simplified ODE converges to a subspace of (\mathbf{W}, \mathbf{H}) satisfying (NC1) and (NC3). Second, they proved that gradient flow, restricted to that subspace, converges to (NC2).

The assumption of small weights and classifiers leading to the linearized ODE is not aligned with today’s paradigm. Specifically, the most commonly used He initialization [He et al., 2015] is designed: (i) to create weights with non-negligible magnitude; and (ii) to preserve the magnitude of features, as they propagate throughout the layers of the network, exactly so that last-layer features would have non-negligible magnitude. Moreover, the analysis of Mixon et al. essentially assumes that (NC1) and (NC3) occur much sooner than (NC2). However, from the experiments in both Pappan, Han, and Donoho [2020] and this paper, there is no empirical evidence that (NC2) happens slower than (NC1) and (NC3) in practice.

E.2 Lu and Steinerberger [2020]

While the MSE loss provides a mathematically natural setting for analysis, the modern paradigm in multi-class classification with deep learning involves training with cross-entropy loss, which is more challenging to analyze than MSE.

Lu and Steinerberger [2020] studied the (one-example-per-class) unconstrained¹⁰ features model with cross-entropy loss:

$$\min_{\mathbf{W}, \mathbf{M}} \text{CrossEntropy}(\mathbf{W}, \mathbf{M}) \quad \text{s.t.} \quad \|\mathbf{w}_c\|_2 = \|\boldsymbol{\mu}_c\|_2 = 1.$$

Since under linear separability the cross-entropy loss can be driven arbitrarily close to zero, just by re-scaling the norms of \mathbf{W} and \mathbf{M} , the authors further imposed a norm constraint on \mathbf{w}_c and $\boldsymbol{\mu}_c$. Lu and Steinerberger observe that the global minimizer of this optimization problem is only achieved once \mathbf{W} and \mathbf{M} are the same Simplex ETF. This derivation is suggestive, but it does not identify closed-form dynamics which would get gradient flow to such a global minimizer, nor does it address the rate of convergence to Neural Collapse. Additionally, the constraint on $\boldsymbol{\mu}_c$ possesses no immediate or direct analogy to standard deep net training—where procedures often control the norm of the weights \mathbf{W} , but not features \mathbf{H} —nor class-means \mathbf{M} .

E.3 E and Wojtowytsch [2020]

E and Wojtowytsch [2020] also consider the unconstrained features model¹⁰ with cross-entropy loss,

$$\min_{\mathbf{W}, \mathbf{H}} \text{CrossEntropy}(\mathbf{W}, \mathbf{H}) \quad \text{s.t.} \quad \|\mathbf{W}\|_2 \leq 1, \|\mathbf{h}_{i,c}\|_2 \leq 1,$$

where they adopt a more technical, *spectral* norm constraint on \mathbf{W} to specify their model.

Building on the results of Chizat and Bach [2018, 2020], E and Wojtowytsch also construct a simple counter-example showing that Neural Collapse need not occur in two-layer, infinite-width networks—which have been the focus of intense recent study in the theoretical deep learning community [Mei et al., 2018, Rotskoff and Vanden-Eijnden, 2018, Arora et al., 2019]. Thus, E and Wojtowytsch’s counterexample suggests the alternative perspective that, despite the expressiveness of infinite-width, two-layer networks, such abstractions do not capture key aspects of trained *deep* nets.

As with Lu and Steinerberger [2020], standard deep net training does not possess any direct analogies for constraining the norm of *features* (as opposed to weights)—nor are there any paradigmatic regularizations that correspond to controlling the *spectral* norm on \mathbf{W} . Moreover, the work does not characterize any closed-form dynamics or the rate of convergence to Neural Collapse.

E.4 Poggio and Liao [2020a,b] (with Banburski)

Distinguished from the simplified unconstrained features models in the previously mentioned works is the theoretical analysis of Poggio and Liao [2020a,b] (in a special section, co-authored with Andrzej Banburski).

The authors study deep homogeneous classification networks, with weight normalization layers, trained with stochastic gradient descent and weight decay. This is much closer to today’s training paradigm, but the setting still differs from the one in which Neural Collapse has been empirically observed in Pappas, Han, and Donoho [2020] and in Section A of this paper. In particular, they replace batch normalization with weight normalization and consider deep homogeneous networks; homogeneous networks can not have bias vectors nor skip connections, which are present both in ResNet and DenseNet. Moreover, the work gives explicit descriptions of neither the dynamics nor the rate of convergence to Neural Collapse.

E.5 Ergen and Pilanci [2020]

While the above-described works tend to focus on either the used-in-practice cross-entropy loss or the theoretically-insightful MSE loss, Ergen and Pilanci [2020] observed that these are both instances

¹⁰The model is unconstrained in the sense that the features are allowed to move directly with gradient flow and are not constrained to be the output of a forward pass—not in the sense that there are no constraints on the optimization problem.

of the general class of convex loss functions and, thus, one could derive insights from the classical convex analysis literature. Moreover, compared to Mixon et al. [2020], Lu and Steinerberger [2020], E and Wojtowytsch [2020], this work studies the optimization starting from the *second*-to-last layer features rather than the last-layer features. In particular, the authors use a strong-duality argument to show that NC emerges in the optimal solution of an equivalent proxy-model to the following optimization:

$$\min_{\mathbf{H}_{L-1}, \mathbf{W}_{L-1}, \mathbf{W}_L, \gamma, \alpha} \mathcal{L} \left(\mathbf{W}_L (\text{BN}_{\gamma, \alpha} (\mathbf{W}_{L-1} \mathbf{H}_{L-1}))_+, \mathbf{Y} \right) + \frac{\lambda}{2} \left(\|\gamma\|_2^2 + \|\alpha\|_2^2 + \|\mathbf{W}_L\|_F^2 \right),$$

where $\mathcal{L}(\cdot)$ is a general convex loss, \mathbf{H}_{L-1} are the second-to-last layer activations, \mathbf{W}_{L-1} are the second-to-last layer weights, \mathbf{W}_L are the network classifiers, \mathbf{Y} are the training targets, λ is a weight-decay parameter, $\text{BN}_{\gamma, \alpha}(\cdot)$ is a batch-norm operator parameterized by α and γ , and $(\cdot)_+$ is a ReLU. The incorporation of batch-normalization and weight-decay ensures the existence of bounded, well-defined optimal solutions—serving a similar role to that of weight-normalization and weight decay in Poggio and Liao [2020a,b] as well as the norm constraints in the other aforementioned related works.

Since strong-duality only characterizes properties of the converged optimal solution of an optimization model, Ergen and Pilanci [2020] does not provide insights into the dynamics with which that solution is achieved which training.

E.6 Fang, He, Long, and Su [2021]

In Fang et al. [2021], the authors introduce the *(N)-layer-peeled model* in which one considers only the direct optimization of the N -th-to-last layer features of a deep net along with the weights that come after the N -th-to-last layer. The motivating philosophy is that, after raw inputs are passed through some initial number of layers, the overparameterization of those layers would allow us to effectively model the N -th-to-last layer features as freely-moving in some subset of Euclidean space. In this terminology, the concurrent works of Mixon et al. [2020], Lu and Steinerberger [2020], E and Wojtowytsch [2020] on the unconstrained (last-layer) features model could be considered instances of a 1-layer-peeled model; while the model of Ergen and Pilanci [2020] could be considered as a 2-layer-peeled model. This perspective is attractive because it gives a name and organization to a common modeling philosophy behind the above-described body of independent works. For comparison, the work of Poggio and Liao [2020a,b] is a non-example of layer-peeled modeling as it considers optimization on the weights of homogeneous deep nets and not the input features.

Fang et al. [2021] then analyzes a convex relaxation of the 1-layer-peeled model—with norm constraints on the weights and features—into a semidefinite program. Not only do the authors show that this model exhibits Neural Collapse in the canonical setting of balanced examples-per-class, but they also analyze the behavior of this model under *imbalanced classes*. While, in the imbalanced case, one would intuitively expect the Simplex ETF to “skew” to have bigger angles around over-represented classes and smaller angles around under-represented ones; Fang et al. [2021] identifies the surprising phenomenon—named *minority collapse*—in their model where, when the imbalances pass a certain threshold, *the last-layer features and classifiers of the under-represented classes collapse to be exactly the same*. However, their work does not provide closed-form dynamics or rates at which collapse—in either the balanced or imbalance case—occurs.

E.7 Zhu, Ding, Zhou, Li, You, Sulam, and Qu [2021]

In Zhu et al. [2021], the authors examine the following unconstrained features model:

$$\min_{\mathbf{W}, \mathbf{H}, \mathbf{b}} \text{CrossEntropy}(\mathbf{W}\mathbf{H} + \mathbf{b}, \mathbf{Y}) + \frac{\lambda_{\mathbf{W}}}{2} \|\mathbf{W}\|_F^2 + \frac{\lambda_{\mathbf{H}}}{2} \|\mathbf{H}\|_F^2 + \frac{\lambda_{\mathbf{b}}}{2} \|\mathbf{b}\|_F^2,$$

where (\mathbf{W}, \mathbf{b}) are the classifier weights and biases, \mathbf{H} are the last layer features, and $(\lambda_{\mathbf{W}}, \lambda_{\mathbf{H}}, \lambda_{\mathbf{b}})$ are weight-decay parameters. On this model, the authors not only prove that all minima exhibit Neural Collapse but also that *all local minima are global minima*. In comparison to our current paper, Zhu et al. [2021] focus on characterizing the landscape of the loss and, thus, do not explore the dynamics and rate at which such minimizers of the loss are achieved.

Zhu et al. [2021] also make notable empirical contributions by conducting a series of experiments on the MNIST and CIFAR10 datasets trained on MLPs, ResNet18, and ResNet50. Their measurements give evidence for the following novel NC-related phenomena in deep classification networks:

1. **NC is algorithm independent:** NC emerges in realistic classification deep net training regardless of whether the algorithm is SGD, ADAM, or L-BFGS.
2. **NC occurs on random labels:** NC emerges even when the one-hot target vectors are completely shuffled.
3. **Width improves NC:** Increasing network width expedites NC when training with random labels.

The authors of Zhu et al. [2021] moreover conducted ablation experiments suggesting that the following substitutions can be made to deep neural net architectures without affecting performance:

1. **Weight-decay substitution:** Replacing (A) weight-decay on the norm of all network parameters with (B) weight-decay just on the norm of the last-layer features and classifiers.
2. **Classifier substitution:** Replacing (A) the last-layer classifiers that are trained with SGD with (B) Simplex ETF classifiers that are fixed throughout training.

While the authors only demonstrated these new behaviors on limited network-dataset combinations, these experiments indeed inspire interesting conjectures about the generalization behavior of deep nets as well as potential architecture design improvements; Zhu et al. [2021] discuss many of these conjectures and related open-questions in detail.